Biomedicine & Pharmacotherapy 200 (2026) 119625

Contents lists available at ScienceDirect

Biomedicine & Pharmacotherapy

journal homepage: www.elsevier.com/locate/biopha

Integrated electrophysiological, cellular, and pharmacological profiling reveals variant-specific mechanisms in SCN4A-related myotonia

Anthony Frosio [a,1], Serena Calamaio [b,1], Serena Pagliarani [c,1], Federica Cirillo [d], Dario Melgari [a], Rachele Prevostini [b], Francesca Lo Presti [a], Sabrina Lucchiari [e], Francesca Magri [c], Stefania Corti [c,e], Giacomo P. Comi [c,e], Luigi Anastasia [a,d], Carlo Pappone [a,d,h], Giovanni Meola [f,g], Ilaria Rivolta [a,b,*]

[a] Institute of Molecular and Translational Cardiology, IRCCS Policlinico San Donato, San Donato Milanese, Italy
[b] School of Medicine and Surgery, University of Milano-Bicocca, Monza, Italy
[c] Foundation IRCCS Ca' Granda Ospedale Maggiore Policlinico, Neurology Unit, Milan, Italy
[d] Faculty of Medicine and Surgery, Vita-Salute San Raffaele University, Milan, Italy
[e] Neuroscience Section, Dino Ferrari Centre, Department of Pathophysiology and Transplantation, University of Milan, Milan, Italy
[f] Department of Neurorehabilitation Sciences, Casa di Cura Igea, Milan, Italy
[g] Department of Biomedical Sciences for Health, University of Milan, Milan, Italy
[h] Arrhythmology Department, IRCCS Policlinico San Donato, San Donato Milanese, Italy

ARTICLE INFO

Keywords:
Myotonia
Patch-clamp
Mexiletine
Myotonia congenita
Trafficking
Sodium channel
ER stress

ABSTRACT

Non-dystrophic myotonias are rare skeletal muscle channelopathies characterized by delayed muscle relaxation and clinical stiffness. This study investigates the molecular mechanisms underlying three missense variants in *SCN4A* encoding for the voltage gated skeletal muscle sodium channel $Na_V1.4$—p.K1308R, p.R1451H, and p.M1701V—identified in patients with non-dystrophic myotonia. All probands carried these variants in combination with the ClC-1 p.G190S mutation, a digenic configuration likely contributing to the heterogeneous clinical manifestations. An integrated approach combining electrophysiology, protein trafficking assessment, and evaluation of endoplasmic reticulum stress, revealed distinct pathogenic signatures for each variant. p.K1308R and p.M1701V primarily altered channel gating, whereas p.R1451H exhibited profound cellular impairment, including intracellular retention, reduced membrane expression, and robust activation of endoplasmic reticulum-stress pathways. Functionally, p.K1308R and p.R1451H caused marked reductions in current density and slowed activation kinetics, while p.M1701V produced milder perturbations consistent with its generally less severe phenotype. Because cold exposure exacerbated symptoms in carriers of p.R1451H and p.M1701V, the functional behaviour of these variants was examined at 37 °C. Both showed recovery of current amplitude to wild-type values and normalization of activation voltage dependence, although inactivation defects persisted. These temperature-dependent improvements were accompanied by increased window current probability, indicating partial temperature-dependent stabilization of channel gating. Pharmacological testing revealed that mexiletine modulates gating abnormalities in a variant-specific manner, reinforcing the clinical relevance of mechanistic stratification. Overall, the findings showed that clinically similar myotonic phenotypes may arise from divergent molecular defects and emphasize the relevance of precision medicine approaches tailored to variant-specific pathogenic mechanisms.

1. Introduction

Non-dystrophic myotonias (NDMs) are rare skeletal muscle channelopathies characterized by myotonia, defined as the delayed relaxation of a muscle after contraction or percussion, and are experienced by patients as muscle stiffness following voluntary movement [1,2].

Myotonia congenita (MC) is the most frequent inherited muscle

* Correspondence to: School of Medicine and Surgery, University of Milano-Bicocca, Via Cadore, 48, Monza, MB 20900, Italy.
E-mail address: ilaria.rivolta@unimib.it (I. Rivolta).
[1] These three authors contributed equally

https://doi.org/10.1016/j.biopha.2026.119625
Received 7 January 2026; Received in revised form 27 May 2026; Accepted 4 June 2026
Available online 6 June 2026

channelopathy [3] caused by mutations in *CLCN1* gene, which encodes the skeletal muscle chloride channel (ClC−1). Myotonia congenita can be inherited in both dominant (Thomsen MC) and recessive (Becker MC) forms. Symptoms are usually prominent in the legs and improve with repeated activity (warm-up phenomenon). Paramyotonia congenita and sodium channel myotonia are dominantly inherited and are caused by mutations in *SCN4A* gene, that encodes the skeletal muscle sodium channel ($Na_V1.4$). The typical features of sodium channel myotonia are involvement of facial muscles, sensitivity to cold and pain [2].

Several treatments are available for NDMs [4]. Mexiletine is a class 1b antiarrhythmic drug that acts by blocking sodium channels and is the first-choice treatment for myotonia [2]. Recently, a systematic review on drug treatment for myotonia reported that mexiletine is likely to reduce myotonia and may improve quality of life compared to placebo [5]. The long-term efficacy and safety of mexiletine treatment in patients with NDMs have also been evaluated, demonstrating no serious adverse events [6,7].

Classical NDMs phenotypes are well characterized but symptoms can overlap, and the wide range of clinical phenotypes and severity makes the diagnosis difficult. For this reason, genetic analysis is an integral part of the diagnostic process. Some pathogenic variants of the *CLCN1* gene have been reported to cause disease when present in both dominant or recessive manner, complicating molecular diagnosis in sporadic patients. Among these variants, p.Gly190Ser is frequently reported in Italian patients with MC [8–13]. Furthermore, there is an increasing number of patients affected by skeletal muscle channelopathies who present digenic variants in the *CLCN1* and *SCN4A* genes [14–18]. Indeed, the coexistence of digenic variants in both *CLCN1* and *SCN4A* genes was observed in 4.5% of a Japanese cohort of NDM patients [19]. Digenic genotypes may lead to a more complex phenotype, broadening the phenotypic and genetic background of these disorders.

We present five myotonic patients belonging to three unrelated families, all carrying the heterozygous p.Gly190Ser in the *CLCN1* gene and a heterozygous variant in the *SCN4A* gene. The p.Gly190Ser variant has already been described and is considered pathogenic based on electrophysiological experiments [9,20].

In this study, we combined complementary experimental approaches to dissect the contribution of SCN4A variants to the phenotype observed in each family. Functional and expression analyses were performed to characterize the impact of the variants, including evaluation of endoplasmic reticulum stress responses and channel trafficking to the plasma membrane. In addition, we assessed the effects of mexiletine and increased temperature on channel behaviour, in order to determine whether these targeted interventions may partially counteract the functional consequences of the variants.

2. Patients and methods

2.1. Patients

All patients provided written informed consent in accordance with the guidelines of the Ethics Committee / IRB: IRCCS Fondazione Ca' Granda Ospedale Maggiore Policlinico (Study code: 0017300 Rebineu).

2.2. Genetic analysis

Genomic DNA was extracted from blood samples using FlexiGene DNA Kit (Qiagen, Hilden, Germany). *CLCN1* and *SCN4A* were analyzed by amplification of PCR fragments containing all the coding exons and intron-exon junctions (primer sequences and conditions are available upon request). Amplicons were sequenced by Sanger method using Big Dye Terminator Cycle Sequencing Kit in an automated sequencer 3130 (Applied Biosystems, Foster City, USA). Sequences were analyzed using SeqScape software (Applied Biosystems) and compared to NCBI sequences NM_000083 and NG_009815 for *CLCN1* and NG_011699 and NM_000334 for *SCN4A*.

2.3. Bioinformatic analysis

Variants were analysed using public databases dbSNP (https://www.ncbi.nlm.nih.gov/snp/) and gnomAD (https://gnomad.broadinstitute.org/) to verify their population frequencies. ClinVar (https://www.ncbi.nlm.nih.gov/clinvar/) and Leiden Open Variation database (https://databases.lovd.nl/shared/genes/SCN4A) were used to identify the previously unreported variants. The following free on-line tools were used to assess pathogenicity prior to functional studies: Mutation Taster (http://www.mutationtaster.org/); Polyphen2 (http://genetics.bwh.harvard.edu/pph2/); CADD (https://cadd.gs.washington.edu/); REVEL (https://sites.google.com/site/revelgenomics/). The funNCion (https://funnc.shinyapps.io/shinyappweb/) provides predictions of functional effects of missense variants in voltage-gated sodium channels (*SCNxA* genes) and calcium channels (*CACNA1x* genes). This tool provides two kinds of predictions: pathogenic versus neutral and loss-of-function (LOF) versus gain-of-function (GOF). Databases and on-line tools were accessed on 1st December 2025.

2.4. Plasmids generation

The wild-type (WT) *SCN4A* cDNA was cloned into mcs1 of pVITRO2-mcs vector (Invivogen, San Diego, USA) as previously described [21]. For the current experiments the GFP cDNA cloned into mcs2 was removed. Site-directed mutagenesis was performed on WT *SCN4A* cDNA to insert the variants of interest using the Quick-change II kit (Stratagene, Santa Clara, USA). Direct sequencing was performed to verify the insertion of the variants (Supplementary Figure S1) and the absence of other unwanted alterations (the complete plasmid sequences are provided in the Supplementary material). Primers used for site-directed mutagenesis are listed in Supplementary Table 1.

2.5. Cell culture, transfection, and temperature or mexiletine incubation conditions

The human embryonic kidney cell line HEK293T (ATCC, Manassas, VA, USA) was maintained under standard culture conditions (37 °C, 5% CO_2) in DMEM/F12 medium (Gibco–Thermo Fisher Scientific Italia, Monza, Italy) supplemented with 10% fetal bovine serum (FBS; Sigma-Aldrich–Merck Life Science, Milan, Italy), 2 mM L-glutamine, and antibiotics (100 U/mL penicillin and 100 μg/mL streptomycin; Euroclone, Pero, Italy).

Transient transfections were performed using the jetPRIME reagent (PolyPlus Transfection; Euroclone, Pero, Italy) according to manufacturer's instructions. Plasmid constructs encoding *SCN4A* (0.5 μg; WT or mutant) and *SCN1B/SCN2B-GFP* construct (0.5 μg) were introduced into cells.

Forty-eight hours (hs) post-transfection, cells were detached using trypsin/EDTA solution (Gibco–Thermo Fisher Scientific Italia, Monza, Italy), centrifuged at 200 × g for 5 min at room temperature (RT), and replated for patch-clamp experiments. To evaluate targeted pharmacological interventions, two parallel conditions were used: recording performed at 37 °C, or recording from cells exposed to 0.1 mM mexiletine hydrochloride (mexiletine, Sigma-Aldrich–Merck Life Science, Milan, Italy) for 24 hs, with matched untreated control. During each experimental session, recordings from the respective groups were carried out in parallel to allow direct comparison under identical recording conditions. Mexiletine was also acutely superfused onto cells followed by washout to confirm complete removal of the compound. The percentage of block was evaluated.

2.6. Functional analysis

Manual whole-cell patch-clamp experiments were performed at RT (22–24 °C). The external standard solution contained (mM): 40 NaCl, 4 KCl, 2 $CaCl_2$, 1 $MgCl_2$, 10 HEPES, 100 N-methyl-D-glucamine (NMDG),

and 5 glucose, adjusted to pH 7.4 with NaOH (305 mOsm/kg H_2O). The intracellular pipette solution contained (mM): 110 CsF, 10 CsCl, 10 NaCl, 10 HEPES, and 10 EGTA, adjusted to pH 7.2 with CsOH (>280 mOsm/kg H_2O). Borosilicate glass pipettes (2–3 MΩ) were pulled using a P−1000 Flaming-Brown micropipette puller (Sutter Instruments, Novato, CA, USA). Series resistance was compensated up to 80% and readjusted before each protocol. Currents were sampled at 50 kHz and low pass filtered at 10 kHz.

The holding potential was –120 mV. Steady-state activation was measured using 50 ms depolarizing pulses from –80 to + 30 mV in 10 mV increments. Steady-state inactivation was assessed with a 100 ms prepulse from –140 to + 10 mV in 10 mV increments, followed by a –10 mV test pulse of 20 ms. Activation and inactivation curves were fitted with a Boltzmann function:

$$y = \frac{1}{1 + \exp\left(\frac{V - V_{1/2}}{k}\right)}$$

where y represents the relative current, V is the membrane potential, $V_{1/2}$ is the half-maximal voltage, and k is the slope factor.

Activation and inactivation kinetics were determined by fitting the rising and the decay phase, respectively, of the peak current with the following standard single-exponential function:

$$y = \sum_{i=1}^{n} A_i e^{\frac{-x}{\tau_i}} + C$$

where y is the current amplitude at time x, t is the time constant, A is the total fitted current, and C is any unfitted residual current.

Late sodium current was quantified as the TTX-sensitive current measured at the end of a 200 ms depolarizing pulse to 10 mV. Recordings were performed in 140 mM NaCl solution (without NMDG), first in the absence and then in the presence of 30 μM tetrodotoxin (TTX; HelloBio, Bristol, UK). The late current was normalized to the peak current and expressed as a percentage.The predicted window current was obtained as previously described [22,23]. In particular, the experimental mean values of voltage of half activation ($V_{1/2}$ACT) and inactivation ($V_{1/2}$INACT), and the respective mean slopes (k_{ACT} and k_{INACT}), were inserted in the following equation:

$$Open\ Probability = \left(\frac{1}{1 + e^{\frac{V_{1/2}ACT - V_m}{k_{ACT}}}} * \frac{1}{1 + e^{\frac{V_{1/2}INACT - V_m}{k_{INACT}}}}\right) * 100$$

The development of the intermediate inactivation was assessed in standard external solution using a two-pulse protocol. A first depolarizing pulse (P1) from –100 mV to –10 mV was applied for 1–1000 ms, followed by a 20 ms return to –100 mV, and a second test pulse (P2) to –10 mV for 20 ms. The normalized P2/P1 current ratio was plotted as a function of P1 duration. Recovery from fast and intermediate inactivation was assessed in standard solution using a two-step protocol consisting of two depolarizing pulses to –10 mV (P1 and P2), separated by a recovery interval at –120 mV of increasing duration (0.1 ms to 1 s). To measure recovery from fast inactivation, P1 and P2 durations were 50 ms and 20 ms, respectively. To measure recovery from intermediate inactivation, P1 duration was increased to 500 ms, while P2 remained 20 ms. The kinetics were determined by fitting with the following double-exponential function:

$$y = \sum_{i=1}^{n} A_{is} e^{\frac{-x}{\tau_s}} + A_{if} e^{\frac{-x}{\tau_f}} + C$$

where the variables and constants are similar to those of the single-exponential function, but the time constant t is split into a slow (t_s) and a fast (t_f) component.

To assess the specific contribution of each variant to the action potential, we applied a previously established protocol based on data from an earlier study [18]. This protocol reproduces the skeletal muscle action potential waveform, enabling us to determine how each variant alters sodium current dynamics throughout the different phases of the action potential. Cells were maintained at a holding potential of –90 mV, and after a rapid depolarization to + 25 mV, the membrane potential was returned to the holding potential within 10 ms. We then calculated time necessary for 30%, 50%, and 90% of the current decay to obtain quantitative parameters.

The use-dependent block induced by 0.1 mM mexiletine was evaluated using a protocol consisting of 10 Hz stimulation from a holding potential of −120 mV, with 25 ms depolarizing pulses to 0 mV, followed by washout to confirm complete drug removal. The percentage reduction in the peak current was then calculated. Extracellular and intracellular solutions were as described above. Data were acquired using a Multiclamp 700B amplifier and Digidata 1550B interface with pClamp 11.2 software, and analyzed with Clampfit 11.2 (Axon Instruments, Molecular Devices, San Jose, CA, USA).

2.7. Protein extraction, membrane isolation and Western blot analysis

HEK293T cells non transfected (NT) or transfected with either WT *SCN4A* or mutant constructs carrying the p.K1308R, p.R1451H, or p.M1701V variants (in all the text we will refer to the aminoacidic substitution in the protein, rather than the base substitution in the gene) were harvested at approximately 80% confluency. Cells were resuspended in phosphate-buffered saline (PBS) supplemented with a protease inhibitor cocktail (Merck, Darmstadt, Germany). Lysis was performed on ice by pulse sonication using 10 pulses of 0.5 s each. The resulting lysates were clarified by centrifugation at 800 × g for 10 min at 4 °C to remove cell debris. Membrane fractions were separated from cytosolic proteins by ultracentrifugation at 37,000 × g for 75 min at 4 °C using an Avanti™ J−30I centrifuge (Beckman Coulter, Brea, CA, USA) and their protein concentrations were determined with the Pierce BCA Protein Assay Kit (Thermo Scientific, Waltham, MA, USA) according to the manufacturer's instructions. All the analysed samples were denatured for 15 min at 55 °C in sample buffer (0.6 g/100 mL Tris, 2 g/100 mL SDS, 10% glycerol, 1% 2-mercaptoethanol, pH 6.8) to preserve the integrity of high-molecular weight proteins, separated on a 6% SDS-PAGE gel, and transferred to nitrocellulose membranes (Trans-Blot, Bio-Rad Laboratories, Segrate, Italy) by electroblotting. To facilitate the transfer of high–molecular-weight proteins, 0.1% SDS was included in the transfer buffer. Membranes were blocked for 1 h at RT in TBS (Tris-HCl, pH 7.5) containing 5% non-fat dry milk and then incubated overnight (O/N) at 4 °C with a primary antibody against Na_V (Monoclonal Anti-Sodium Channel, Pan antibody, mouse K58/35, monoclonal, Sigma St Louis, MO, USA; dilution 1:200). After washing three times with TBS containing 0.1% Tween−20 (TBS-T), membranes were incubated for 1 h at RT with an HRP-conjugated secondary antibody. NCAM1, which has a molecular weight of approximately 150 kDa, was used as an internal reference control and displayed a consistent and stable band across all samples, supporting equal loading and transfer efficiency (see Supplementary Figure S4). Signal detection was performed using the ECL detection kit (Cyanagen, Bologna, Italy), according to manufacturer's protocol. Membranes were imaged using the LI-COR Odyssey Infrared Imaging System, and band intensities were quantified with Image Studio Lite software (LI-COR Biotechnology, Lincoln, NE, USA). Relative protein levels were normalized to total protein using the REVERT Total Protein Stain Kit (LI-COR Biotechnology), following the manufacturer's instructions.

2.8. Immunofluorescence, image acquisition, processing and quantification

Immunofluorescence was performed as previously described [24] on HEK293T cells transfected with either WT *SCN4A* or mutant constructs

encoding for the p.K1308R, p.R1451H, or p.M1701V variants. NT cells served as negative control. Cells were seeded on 13 mm glass coverslips, fixed with 4% paraformaldehyde, permeabilized, and blocked prior to O/N incubation with monoclonal pan-sodium channel antibody (mouse K58/35, Sigma St Louis, MO, USA; dilution 1:200). After washing, cells were incubated 1 h with donkey anti-mouse Alexa Fluor 594-conjugated secondary antibody (Invitrogen, Waltham, MA, USA), followed by nuclear counterstaining with 4′,6-diamidino−2-phenylindole (DAPI) and mounting. Confocal images for assessing subcellular channel localization were acquired using a Zeiss LSM710 microscope (63 × oil immersion objective, Airyscan Z-stack acquisition) and processed with Zeiss ZEN and ImageJ software. Mean fluorescence intensity (MFI) was quantified from Airyscan-processed image stacks by converting image to 8-bit, generating a maximum-intensity Z-projection, tracing the entire cell membrane, extracting the membrane intensity profile, averaging its values, and subtracting the mean background intensity calculated from five cell-free regions. For each condition, at least 10 individual cells were analyzed.

Additional channel subcellular localization was quantified as the F_{PN}/F_{PM} ratio, calculated by dividing the MFI at the perinuclear ring (F_{PN}) by the corresponding intensity at the plasma membrane (F_{PM}). For each cell, F_{PN} was obtained as the mean of ten fixed-area regions sampled along the perinuclear ring, whereas F_{PM} was obtained from the average membrane MFI measured along the plasma membrane perimeter for the same cell.

2.9. Transfection efficiency and morphological analysis

Transfection efficiency and cell morphology were assessed by wide-field fluorescence imaging. Images were acquired for nuclear counting and morphological analysis using a Leica Thunder Imager System (40 × objective; Leica Microsystems, Wetzlar, Germany). For each coverslip, 3 × 3 mosaic images were collected from at least three distinct regions. Image analysis was performed with ImageJ.

Transfection efficiency was determined as the percentage of DAPI-positive nuclei exhibiting red fluorescence ($Na_V1.4$-positive cells) relative to the total number of nuclei. For this purpose, the blue (DAPI) and red ($Na_V1.4$ transfection marker) channels were processed independently using an identical workflow. Briefly, images were converted to 8-bit grayscale, and an intensity threshold was defined using the Otsu automatic method on representative WT images. Because all images were acquired under identical exposure conditions, the same threshold values were applied across all experimental groups ($Na_V1.4$ WT, p.K1308R, p.R1451H, and p.M1701V), ensuring consistent segmentation. Following thresholding, images were binarized and subjected to erosion and watershed operations to refine object boundaries and separate adjacent structures. Channel-specific size filters were applied prior to segmentation. The total number of nuclei (N) and red-positive cells (T) were quantified for each image, and transfection efficiency was calculated as:

$$\%\text{transfected} = \frac{T}{N} \times 100$$

Cell morphology was assessed exclusively in transfected cells using binary masks derived from the red channel. Shape descriptors were used to classify cells as spherical or elongated. Circularity was defined as 4π × (area/perimeter), with values ranging from 0 (linear object) to 1 (perfect circle). The aspect ratio was calculated as the ratio between the major and minor axes of the best-fitting ellipse, with higher values indicating increased elongation [25,26].

2.10. Quantitative real-time PCR (RT-qPCR)

Total cellular RNA was extracted using the ReliaPrep™ RNA Cell Miniprep System (Promega, Madison, WI, USA), including an on-column DNase treatment, according to the manufacturer's instructions. RNA concentration and purity were assessed with a NanoDrop spectrophotometer (Thermo Fisher Scientific). Reverse transcription was carried out with 1 µg of total RNA using the iScript™ cDNA Synthesis Kit (Bio-Rad).

For RT-qPCR, cDNA was amplified in the presence of GoTaq® qPCR Master Mix (Promega), specific primers (previously described [27] and listed in Supplementary Table 2), and RNase-free water. Reactions were run on a CFX Opus 96 Real-Time PCR System (Promega) with the following cycling protocol: 95 °C for 2 min, followed by 39 cycles at 95 °C for 15 s and 60 °C for 1 min (with fluorescence acquisition at the 60 °C step). A final melt curve analysis was performed from 60 °C to 95 °C, increasing by 0.5 °C per cycle, with continuous plate reading.

Mean cycle threshold (Ct) values were normalized to endogenous reference genes (*GAPDH* and *ACTB*) or *SCN4A* against cells transfected with the same amount of plasmid DNA. Relative expression levels were calculated using the comparative ΔCt and ΔΔCt methods data are presented as fold change relative to NT (set to 1), calculated using the $2^{-\Delta\Delta Ct}$ method and normalized to *ACTB* and *GAPDH*. The NT condition in the graph appears without variability because it represented the reference condition.

2.11. Statistical analysis

Functional, morphological, and molecular data are presented as mean ± SEM from technical triplicates and at least three independent biological replicates derived from independent transfections (n = number of cells). Statistical analyses were performed using OriginPro 2016 (OriginLab, Northampton, MA, USA) or Prism (GraphPad, San Diego, CA, USA).

Functional recordings analysis was performed using two-way ANOVA with a modified *t*-test and Fisher's correction or Student's *t*-test (OriginPro 2016). For the morphological analysis of transfected cells and for RT-qPCR reactions, data distributions were first assessed for normality using the Shapiro–Wilk test. Normally distributed datasets were analysed using Student's unpaired *t*-test, whereas non-normal morphological datasets (morphometric parameters) were evaluated using the non-parametric Mann–Whitney test. qPCR datasets satisfied normality and were analysed per comparison using Student's unpaired *t*-test.

Across all analyses, significance thresholds were set at $p < 0.05$, with significant values indicated in figures and tables using condition-specific symbols, the details of which are provided in the corresponding legends.

3. Results

3.1. Family 1

The proband of family 1 was a man presenting with stiffness after rest starting in childhood. On clinical examination, percussion myotonia and eyelid myotonia were evoked. Lid-lag and warm-up phenomenon were present. Electromyography (EMG) showed myotonic discharges and creatine kinase (CK) levels were slightly elevated. Genetic analysis disclosed the heterozygous NM_000083:c.568_569delinsTC, p.(Gly190Ser) (also previously reported as c.568GG>TC, G190S) in exon 5 of the *CLCN1* gene and the unreported heterozygous NM_000334:c.3923 A>G, p.(Lys1308Arg, K1308R) in exon 22 of *SCN4A* gene. This variant is not reported in gnomAD, dbSNP, Leiden database or ClinVar and was predicted to be pathogenic by four out of five prediction tools (Table 1). Lysine 1308 is conserved among species but, interestingly, all the Na_V channels harbour glutamine at this position (Supplementary Figure S2). After the application of the American College of Medical Genetics and Genomics (ACMG) rules, the p.(Lys1308Arg) was classified as variant of uncertain significance (VUS; PM1, PM2_sup).

Table 1
In silico prediction tools results (GOF: gain of function; prob: probability).

VARIANT	POLYPHEN 2	MUTATION TASTER	funNCion	CADD	REVEL
p.K1308R	Possibly damaging (score 0.59)	Disease causing (prob 0.99)	Pathogenic (prob 0.60); GOF (prob 0.76).	25.7	0.59
p.R1451H	Probably damaging (score 0.99)	Disease causing (prob 0.99)	Pathogenic (prob 0.98); GOF (prob 0.51).	26.7	0.99
p.M1701V	Probably damaging (score 1)	Disease causing (prob 0.99)	Pathogenic (prob 0.51); GOF (prob 0.67).	24	0.85

3.2. Family 2

The proband of family 2 was a woman in her late fifties, who experienced important stiffness at lower limbs and hands, associated with muscle cramps and myalgia in the hands. Symptoms were exacerbated by cold and began at 9 years of age. On clinical examination, the proband presented with eyelids, hands, and lower limbs myotonia, mild proximal weakness in all four limbs and selective hypertrophy of thighs. No tongue myotonia was elicited but patient reported difficulties in chewing. The warm-up phenomenon was present. The patient complained of muscle fatigue and tiredness upon awakening, but she never had episodes of paralysis. EMG showed myotonic discharges. CK levels and cardiac assessments were normal. The proband mother showed the same symptoms, and the maternal grandfather complained about muscle stiffness in his hands. The proband had two children, both symptomatic.

The proband's son, aged 28, complained of muscle cramps and stiffness from the age of 14. At neurological evaluation generalized muscle hypertrophy was evident and myotonia was elicited in the hands, lower limbs and eyelids. EMG showed myotonic discharges. CK levels were elevated (750 IU/L). Cardiac assessments were normal.

The proband's daughter, aged 36, presented with a milder involvement. She complained of stiffness in her hands since adolescence, which was not exacerbated by cold. On physical examination, percussion myotonia in her hands was present, but inconstant. EMG showed myotonic discharges. CK levels and cardiac evaluation were normal.

In the proband, myotonic dystrophy type 1 (DM1) was excluded by the analysis of *DMPK* gene. Genetic analysis of *CLCN1* gene revealed the heterozygous NM_000083:c.568_569delinsTC, p.(Gly190Ser) on exon 5.

Segregation studies revealed the p.(Gly190Ser) variant in both the proband's son and mother, but not in the daughter. This result prompted us to analyse *SCN4A*. The analysis disclosed the heterozygous variant NM_000334:c.4352 G>A p.(Arg1451His, R1451H) in the proband and in both her children. The proband's mother was not available for the segregation study for the p.(Arg1451His) variant.

c.4352 G>A is located in exon 24 and R1451 is the second arginine of voltage sensor DIV-S4 [28]. Demonstrating the importance of this amino acid, all Na_V channels harbour arginine at this position, which is also conserved among $Na_V1.4$ channels from other species (Supplementary Figure S2). p.(R1451H) is reported in dbSNP (rs748517635), in ClinVar (448280) with conflicting classification, and in the Leiden database as VUS. It is described in gnomAD with a frequency of 8.505e−7 in the European population. All in silico prediction tools used returned a pathogenic score (Table 1). The application of ACMG rules led to classification of this variant as pathogenic (PS4, PM1, PM2_sup, PM5, PP1, PP3).

3.3. Family 3

A 30-years-old woman presented with cold-induced myalgia and muscle cramps in the quadriceps and hands, which began at age 22. Clinical evaluation disclosed mild myotonia in both hands, quadriceps and tongue. Weakness was absent. CK levels were normal or mildly elevated. EMG showed myotonic discharges without myopathic changes. The proband's mother complained about stiffness in the lower limbs that began during childhood. No clinical myotonia was evoked at clinical examination even though EMG showed myotonic discharges. Genetic analysis revealed in both the proband and the mother the heterozygous NM_000083:c.568_569delinsTC, p.(G190S) on the *CLCN1* gene and the novel heterozygous variant NM_000334:c.5101 A>G, p.(Met1701Val, M1701V) on exon 24 of *SCN4A* gene. Methionine at amino acid 1701 in $Na_V1.4$ is not conserved in fish while all Na_V channels harbour methionine at this position (Supplementary Figure S2). This variant is described in gnomAD with an allele frequency of 8.476e−7 in the European population and in dbSNP (rs1270081591). It is not present in Clinvar or the Leiden database. The prediction tools expected this variant to be pathogenic (Table 1). ACMG criteria were applied and p.(Met1701Val) was classified as a VUS (PM2_sup, PP1, PP3).

3.4. Functional characterization

The electrophysiological properties of the $Na_V1.4$ mutants p.K1308R, p.R1451H, and p.M1701V were characterized in HEK293T cells and compared with those of the $Na_V1.4$ WT channel. A summary of the experimental data is presented in Fig. 1, Table 2**A**, and Supplementary Figure S3.

Among the three variants examined (representative traces in Fig. 1**A**), p.K1308R and p.R1451H showed a robust and statistically significant reduction in current density relative to the WT, whereas p.M1701V exhibited only a non-significant trend towards lower values (Fig. 1**B**). All three $Na_V1.4$ variants affected the voltage dependence of activation or inactivation (representative traces Fig. 1**C, D**). However, only p.K1308R and p.R1451H produced significant shifts in the activation curve toward more depolarized potentials, by approximately + 3.7 mV and + 6.4 mV, respectively, whereas p.M1701V did not induce a significant change. In addition, the p.R1451H variant caused a significant increase in the activation slope factor (Table 2**A**).

Regarding the voltage dependence of inactivation, only the p.M1701V mutation induced a depolarizing shift of the steady-state inactivation curve (approximately +4.1 mV), while p.R1451H significantly increased the inactivation slope factor (Table 2**A**). The time course of channels activation and inactivation are shown in Fig. 1**E** and Fig. 1**F**. Both p.K1308R and p.R1451H exhibited slower activation compared with the WT channel, whereas p.R1451H and p.M1701V also showed a significant slowing of inactivation kinetics (Table 2**A**).

Late sodium current quantification showed a significant reduction only for the p.M1701V variant relative to the wild type (Supplementary Figure S3A), whereas in the other mutations this parameter remained unchanged.

The window conductance was estimated using Boltzmann-derived activation and inactivation parameters ($V_{1/2}$ and k, Fig. 1**G**). p.R1451H and p.M1701V induced a marked depolarizing shift of the predicted window current, together with an increased probability of its occurrence. In contrast, p.K1308R shifted it toward more hyperpolarized potential without affecting its overall probability (Table 2**A**).

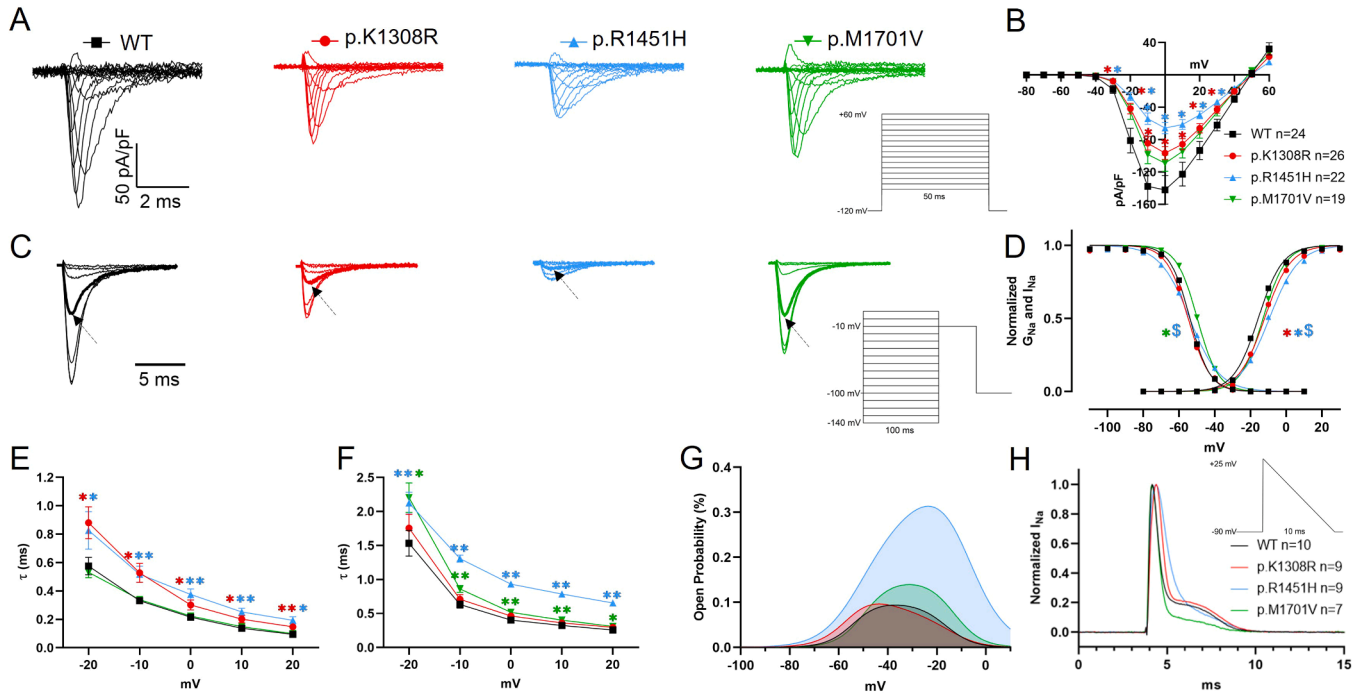

Fig. 1. Electrophysiological characterization of $Na_V1.4$ variants. (A) Representative current traces for the WT (black), p.K1308R (red), p.R1451H (blue), and p.M1701V (green) channels elicited by the reported protocol. (B) Current–voltage (I–V) relationships illustrating the reduction in the mean current density observed for p.K1308R and p.R1451H mutants with respect to the WT channel. (C) Representative traces obtained from the test pulse of the reported steady-state inactivation protocol; for reference, the dashed arrow indicates the current (thicker trace) recorded in response to a prepulse at −50 mV. (D) Activation and inactivation curves were fitted using the Boltzmann equation (see Patients and Methods), yielding the midpoint potentials (V½) and slope factors (k) summarized in Table 2A. (E) Kinetics of channel activation and (F) fast inactivation determined as described in Patients and Methods. (G) Calculated window current expressed as open probability (see Patients and Methods and Table 2A for summarized data). (H) Overall sodium channel contribution elicited by an action-potential shaped voltage protocol (reported). Data are shown as mean ± SEM. Statistical significance: * $p < 0.05$, ** $p < 0.01$, *t*-test analysis. In panel D, * is referred to the V1/2, while $ to the slope factor k. Each construct is identified with a colour code maintained also in the symbols to facilitate the interpretation.

Fig. 1**H** shows the action potential-shaped protocol used to evaluate sodium current throughout the full-time course of an action potential (AP), rather than only the transient component underlying the upstroke. Consistent with their slowed activation kinetics, p.K1308R and p.R1451H reduced the rate at which the elicited sodium current developed. Analysis of the repolarization phase revealed that the p.R1451H variant significantly increased the contribution of the sodium current to AP repolarization at the time points corresponding to 30% and 50% decay of the sodium current. In contrast, the p.M1701V variant showed an early cessation of this contribution, with a ~90% reduction already 1.14 ms after the onset of sodium-current inactivation. In the WT channel, a comparable decrease was observed at 2.64 ms (Table 2**A**). Finally, both p.R1451H and p.M1701V affected also the development of the intermediate inactivation (Supplementary Figure S3B), accelerating the entry in the intermediate state. The recovery from intermediate and fast inactivation (Supplementary Figure S3C and S3D) was not significantly altered by any of the variants.

3.5. Expression level and cellular phenotype of $Na_V1.4$ WT and mutant variants in HEK293T Cells

To assess the impact of $Na_V1.4$ variants on channel expression and on cellular morphology, we quantified mRNA, protein abundance, membrane localization, and morphometric features after transfection in HEK293T cells. As expected, all transfected conditions produced higher *SCN4A* mRNA levels than NT controls. Relative to WT, p.K1308R exhibited comparable mRNA expression (94%), whereas p.R1451H showed a marked reduction (23.5%), and p.M1701V a substantial increase, reaching approximately 3.47-fold higher levels. (Fig. 2**A**).

Western blotting detected $Na_V1.4$ protein at ~250 kDa in whole cell lysate (data not shown) and in membrane-enriched fractions in all conditions (Fig. 2**B**), consistent with the physiological channel membrane localization. NCAM1 detection (MW 150 kDa) was used to supported equal loading and transfer efficiency of high molecular weight proteins (Supplementary Figure S4). Analysis revealed a marked decrease in membrane accumulation for p.R1451H (−50%), whereas p.M1701V showed enhanced abundance (+40%) relative to WT; p.K1308R remained comparable (Figs. 2**B,** 2**C**).

Confocal fluorescence imaging validated these findings, revealing a significant reduction in membrane-associated mean fluorescence intensity in p.R1451H (57%), whereas p.K1308R showed a non-significant decrease (66%) and p.M1701V exhibited levels comparable to the reference condition (WT). (Figs. 2**D,** 2**E**).

To assess whether the presence of the variants could broadly affect the channel trafficking to the plasma membrane, we calculated the fluorescence intensity ratio between the perinuclear ring (F_{PN}) and the plasma membrane (F_{PM}), with higher values indicating reduced delivery to the membrane, hence intracellular protein retention. Transfected cells generally showed elevated F_{PN}/F_{PM} ratios, consistent with substantial ER retention. The mutant proteins p.K1308R (3.4 ± 0.4) and p.M1701V (4.7 ± 0.7) did not differ significantly from WT (3.7 ± 0.5) (see Fig. 2**F** caption for values) indicating comparable trafficking. In contrast, the p.R1451H (9.7 ± 1.4) displayed a 2.8 higher ratio, demonstrating strong intracellular retention (Fig. 2**F**).

Cells overexpressing mutant constructs displayed a more rounded morphology than non-transfected cells and those expressing the WT channel. To quantify this observation, morphometric analysis was performed, revealing variant-specific effects. Expression of p.R1451H and p.M1701V was associated with increased circularity (0.83 ± 0.01 and 0.84 ± 0.01, respectively) and decreased aspect ratio (1.26 ± 0.01 and

Table 2
Quantitative functional analysis of the electrophysiological parameters of the three $Na_V1.4$-variants respect to the WT channel from recordings performed at room temperature (A), at 37°C (B), and (C) after 24 h incubation with 0.1 mM mexiletine; n indicates the number of cells tested from a minimum of three different experiments. Data are shown as mean ± SEM.

		WT	p. K1308R	p. R1451H	p. M1710V
(A) Parameters obtained from recordings @ RT					
Current density @ 0 mV(pA/pF)	(pA/pF)	−142.52 ± 2 (n = 24)	−96.5 ± 8** (n = 26)	−65.5 ± 7** (n = 22)	−109.1 ± 10 (n = 19)
τ fast activation @ 0 mV	(ms)	0.2 ± 0.02 (n = 24)	0.3 ± 0.03* (n = 26)	0.4 ± 0.04** (n = 22)	0.2 ± 0.01 (n = 19)
τ fast inactivation @ 0 mV	(ms)	0.4 ± 0.02 (n = 24)	0.5 ± 0.04 (n = 26)	0.9 ± 0.02** (n = 22)	0.5 ± 0.03** (n = 19)
Late Sodium current	%	2.8 ± 0.4 (n = 13)	2.2 ± 0.6 (n = 13)	2.4 ± 0.3 (n = 12)	1.6 ± 0.3* (n = 11)
Activation	$V_{1/2}$ (mV)	−15.7 ± 1 (n = 24)	−12.0 ± 1* (n = 26)	−9.3 ± 1** (n = 22)	−12.9 ± 1 (n = 19)
	k	5.6 ± 0.3	6.5 ± 0.3	7.4 ± 0.3**	5.7 ± 0.2
Inactivation	$V_{1/2}$ (mV)	−53.9 ± 0.5 (n = 24)	−54.9 ± 0.6 (n = 26)	−54.1 ± 0.7 (n = 22)	−49.8 ± 0.5** (n = 19)
	k	−5.4 ± 0.2	−5.8 ± 0.2	−8.3 ± 0.2#	−5.7 ± 0.3
Window current open probability	(%)	0.09	0.09	0.31	0.13
Window peak voltage	(mV)	−37.1	−43.6	−23.5	−31.3
Time @30% of current decay	ms	0.25 ± 0.01	0.24 ± 0.02	0.4 ± 0.03**	0.22 ± 0.03
Time @50% of current decay	ms	0.38 ± 0.02	0.37 ± 0.03	0.63 ± 0.04**	0.33 ± 0.01
Time @90% of current decay	ms	2.64 ± 0.4	2.92 ± 0.4	2.40 ± 0.2	1.14 ± 0.3*
Recovery from Intermediate Inactivation	τ_f (ms)	1.6 ± 0.1 (=16)	1.7 ± 0.1 (n = 13)	1.6 ± 0.1 (n = 14)	1.4 ± 0.1 (n = 11)
	τ_s (ms)	147.4 ± 11	140.8 ± 12	152.8 ± 13	146 ± 15
(B) Parameters obtained from recordings @ 37 °C					
Current density @ 0 mV (pA/pF)	(pA/pF)	−116.98 ± 9.7 (n = 17)	N/A	−109.6 ± 11£ (n = 19)	−113.8 ± 15 (n = 16)
τ fast activation @ 0 mV	(ms)	0.13 ± 0.02	N/A	0.13 ± 0.01+ £	0.14 ± 0.02£
τ fast inctivation @ 0 mV	(ms)	0.17 ± 0.01	N/A	0.37 ± 0.02£	0.25 ± 0.02+ £
Activation	$V_{1/2}$ (mV)	−15.66 ± 1.4	N/A	−12.8 ± 1£	−15.5 ± 1
	k	5.55 ± 0.4	N/A	6.3 ± 0.4£	4.9 ± 0.4
Inactivation	$V_{1/2}$ (mV)	−51.44 ± 0.4	N/A	−52.5 ± 1.1	−48.5 ± 1.4
	k	−6.04 ± 0.4	N/A	−7.9 ± 0.3+	−5.7 ± 0.4
Window current open probability	(%)	0.20	N/A	0.39	0.20
Window peak voltage	(mV)	−27.8	N/A	−20.9	−23.9
(C) Parameters obtained from recordings in presence of 0.1 mM mexiletine					
Current density @ 0 mV (pA/pF)	(pA/pF)	−110.3 ± 11 (n = 22)	−101.3 ± 11 (n = 21)	−43.7 ± 5 (n = 21)	−115.3 ± 10 (n = 20)
τ fast activation @ 0 mV	(ms)	0.26 ± 0.03	0.38 ± 0.03	0.38 ± 0.03	0.25 ± 0.01
τ fast inctivation @ 0 mV	(ms)	0.40 ± 0.03	0.55 ± 0.04	1.05 ± 0.04*	0.53 ± 0.03
Activation	$V_{1/2}$ (mV)	−9.2 ± 1**	−6.5 ± 1**	−5.3 ± 1**	−9.8 ± 1*
	k	6.5 ± 0.3	6.6 ± 0.3	8.5 ± 0.3*	6.2 ± 0.3

Table 2 (*continued*)

		WT	p. K1308R	p. R1451H	p. M1710V
(A) Parameters obtained from recordings @ RT					
Inactivation	$V_{1/2}$ (mV)	−52.2 ± 0.5	−50.9 ± 0.5**	−52.3 ± 0.9	−48.3 ± 0.6
	k	−5.5 ± 0.2	−5.5 ± 0.2	−8 ± 0.3	−4.9 ± 0.1*
Window current open probability	(%)	0.086	0.074	0.305	0.118
Window peak voltage	(mV)	−42.7	−41.8	−34.3	−41.5

(A), * indicate $p < 0.05$, ** indicates $p < 0.01$ vs. WT, respectively; (B) + indicates $p < 0.05$ vs. WT recorded at RT and £ $p < 0.05$ vs same variant at room temperature; (C) *, ** indicate $p < 0.05$ and $p < 0.01$, respectively, vs. corresponded variant recorded without mexiletine incubation.

1.27 ± 0.01) relative to WT cells (circularity 0.81 ± 0.01; aspect ratio 1.39 ± 0.01), consistent with a more rounded phenotype (Figs. 2**G,** 2**H**). In contrast, p.K1308R produced only modest changes compared with WT (circularity, 0.85 ± 0.01; aspect ratio, 1.28 ± 0.03). These morphological differences were not accompanied by changes in membrane surface area, as indicated by comparable whole-cell capacitance measured by patch clamp (WT, 18.2 ± 0.9 pF, n = 24; p.K1308R, 18.1 ± 1.0 pF, n = 26; p.R1451H, 17.3 ± 0.8 pF, n = 22; p.M1701V, 18.2 ± 1.0 pF, n = 19).

Although these morphological alterations are not diagnostic, they are frequently associated with changes in cellular stress states [29]. Notably, transfection efficiency was markedly reduced for all variants (p.K1308R: 1.3%; p.R1451H: 1.6%; p.M1701V: 1.7%) compared to the WT (4.3%), suggesting potential differences in cellular tolerance to expression of mutant channel. In light of this observation, the involvement of the endoplasmic reticulum (ER) stress response was subsequently investigated.

3.6. ER stress response in HEK293T cells expressing WT and mutant $Na_V1.4$ Channels

It is known that the modification in protein synthesis can induce ER stress [30]; thus, the overall impact of $Na_V1.4$ overexpression of WT or mutant on ER stress was assessed, using NT cells as reference. Activation of the unfolded protein response (UPR) was evaluated by measuring multiple markers corresponding to the three major signalling branches of ER stress activation, including *XBP1* (spliced -s*XBP1*-, unspliced -us*XBP1*-, and total*XBP1*), *ATF4*, *DDIT3*-CHOP, and *HSPA5*-BiP (Fig. 3**A**).

qPCR data were normalized to housekeeping genes, and as shown in Supplementary Figure S5A. s*XBP1* levels increased in all transfected conditions compared with NT controls (WT: 4.89 ± 1.54-fold; p.K1308R: 4.23 ± 1.04-fold; p.R1451H: 3.11 ± 0.59-fold; p.M1701V: 3.71 ± 1.66-fold), suggesting that transfected cells were experiencing ER stress and had activated the UPR. This finding was not unexpected, as the high protein production rates associated with overexpression systems may impair ER homeostasis. [31].

Because the initial qPCR measurements reflected the average signal from a mixed population of transfected and non-transfected cells—and, as described above, transfection efficiency was very low, all ER-stress–related transcripts were normalized to *SCN4A* mRNA levels. This approach enabled selective assessment of ER stress activation in the subset of cells effectively expressing the $Na_V1.4$ constructs (Fig. 3; data for the total cell population are reported in the Supplementary Materials **and** Supplementary Figure S5).

Among the three variants tested, p.R1451H produced the most pronounced response, significantly increasing all *XBP1* transcript forms relative to WT: s*XBP1* (3.95 ± 0.91-fold), us*XBP1* (4.50 ± 0.95-fold),

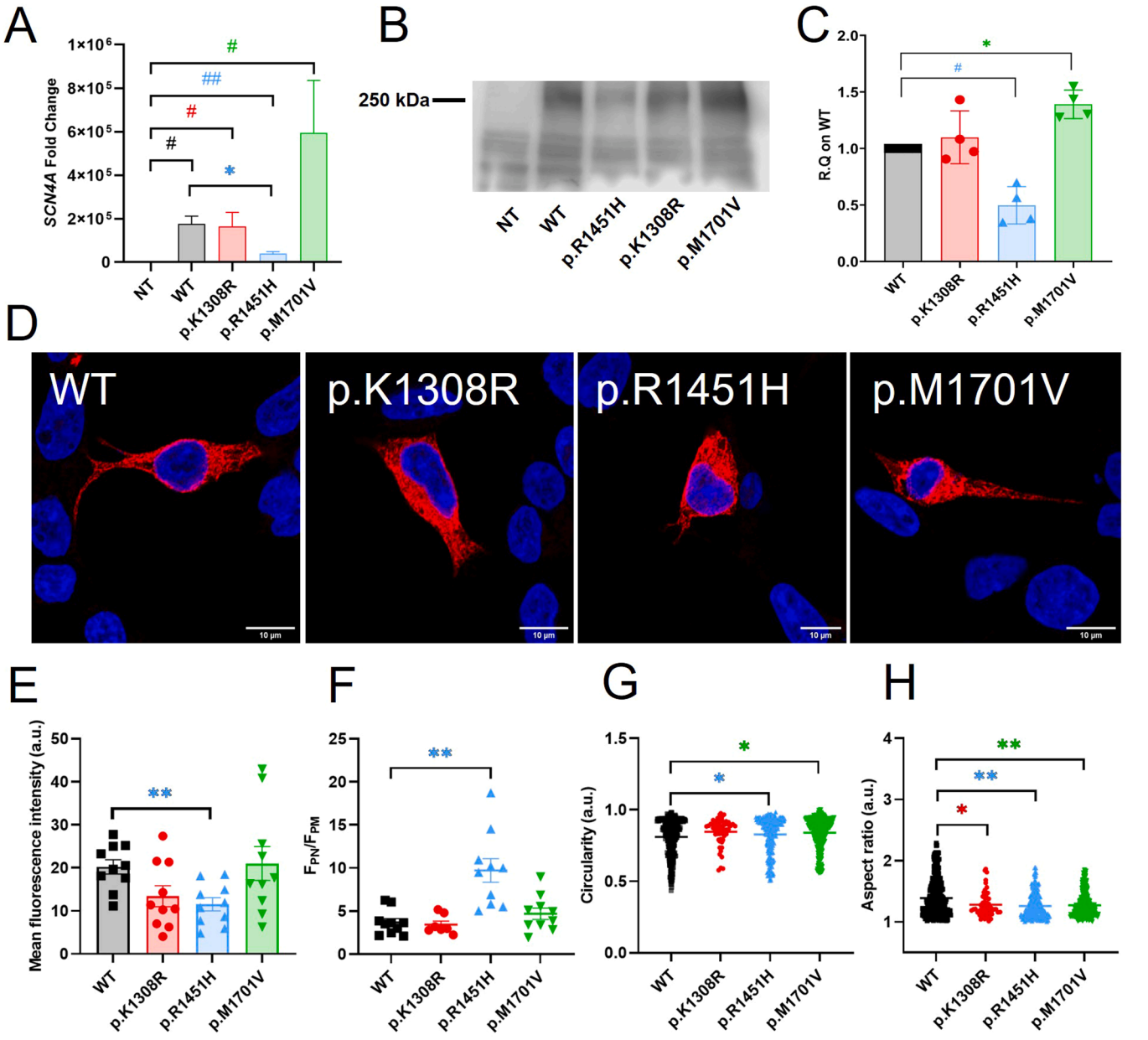

Fig. 2. Expression and cellular phenotype of *SCN4A*/$Na_V1.4$ WT and mutant variants in HEK293T cells. (A) Quantitative PCR analysis of *SCN4A* mRNA levels in non-transfected (NT, white), WT, (grey), and mutant conditions p.K1308R (red), p.R1451H (blue), p.M1701V (green). Data are expressed as fold change relative to NT. All transfected samples show increased *SCN4A* mRNA compared to NT, although p.R1451H displays reduced expression relative to WT ($N \geq 3$ independent transfection). Absolute mean values were $1.7 \times 10^5 \pm 0.6 \times 10^5$ for WT, $1.6 \times 10^5 \pm 1.1 \times 10^5$ for p.K1308R, $0.4 \times 10^5 \pm 0.2 \times 10^5$ for p.R1451H, and $5.9 \times 10^5 \pm 4.2 \times 10^5$ for p.M1701V. (B) Representative western blot showing $Na_V1.4$ protein expression in the membrane fractions obtained by HEK293T cells transfected with WT, and mutant plasmids compared to NT cells. The immunoreactive band corresponding to $Na_V1.4$ was detected at ~250 kDa. (C) Quantification of $Na_V1.4$ abundance in plasma membrane enriched fractions, expressed as relative quantification (R.Q) respect to WT. Reduced membrane accumulation is observed in p.R1451H, while p.M1701V shows enhanced amount of protein; p.K1308R is comparable to WT. ($N = 3$ independent transfections). (D) Representative confocal fluorescence images of HEK293T cells overexpressing $Na_V1.4$ WT or mutants, immunostained for $Na_V1.4$ (red) and counterstained with DAPI (blue). Images represent maximum-intensity projections (4-plane Z-stacks). Scale bar: 10 µm. (E) Quantification of membrane-associated MFI from the variants shown in panel (D). p.R1451H exhibits reduced MFI (10.57 ± 1.5) relative to WT (20.2 ± 1.7), while p.K1308R and p.M1701V did not significantly differ (13.4 ± 2.4 and 21.0 ± 3.9, respectively). (F) MFI expressed as F_{PN}/F_{PM} ratio with values comparable for WT (3.7 ± 0.5), p.K1308R (3.4 ± 0.4), and p.M1701V (4.7 ± 0.7), whereas p.R1451H exhibited an increased ratio (9.7 ± 1.4) consistent with its increased presence in the perinuclear area. (G-H): Morphometric quantification of circularity and aspect ratio in transfected cells revealing that p.R1451H and p.M1701V displayed increased circularity and reduced aspect ratio, consistent with a more rounded phenotype, while p.K1308R showed mild but detectable shifts compared to WT. Effect sizes reported as mean ± SEM. Significance levels: * $p < 0.05$; ** $p < 0.01$ respect to WT; # $P < 0.05$, ## $p < 0.01$ respect to NT.

and total*XBP1* (4.54 ± 0.96-fold) (Fig. 3**B–3D**). Despite this global upregulation, the s*XBP1*/us*XBP1* ratio was reduced (WT: 0.59 ± 0.07; R1451H: 0.50 ± 0.04; Supplementary Figure S5H), indicating decreased *XBP1* splicing efficiency. Consistent with activation of the IRE1α–XBP1 axis, R1451H expression also significantly increased *DDIT3*/CHOP (2.41 ± 0.12-fold) and *HSPA5*/BiP (2.74 ± 0.22-fold) (Figs. 3**F**, 3**G**).

In contrast, p.K1308R induced only mild, non-significant changes in *XBP1* expression (s*XBP1*: 2.05 ± 0.90-fold; us*XBP1*: 2.56 ± 1.18-fold;

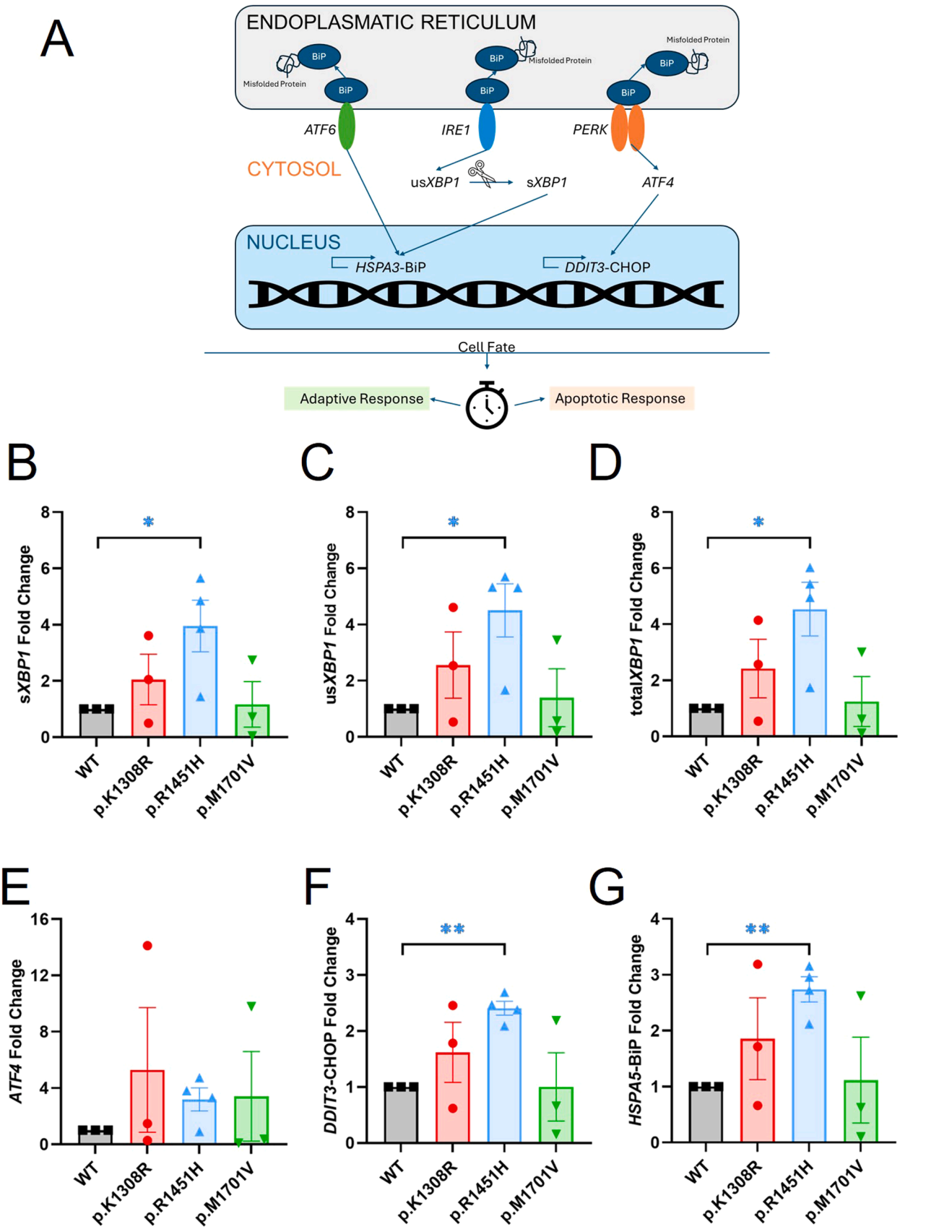

(caption on next page)

Fig. 3. ER stress–related gene expression in HEK293T cells expressing WT or mutant $Na_V1.4$ channels. (A) Schematic representation of major unfolded protein response (UPR) signalling branches. (B-G) Quantitative PCR analysis of ER stress markers in HEK293T cells transiently expressing WT SCN4A (grey) or the p.K1308R (red), p.R1451H (blue), and p.M1701V (green) variants. (B-D) The p.R1451H variant significantly increases the expression of s*XBP1*, us*XBP*, and total*XBP1* transcript levels compared to WT, while p.K1308R and p.M1701V do not differ significantly, although p.K1308R shows a slight increase. (E-G) The p.R1451H variant significantly enhances *DDIT3-CHOP* and *HSPA5-BiP* expression compared to WT, while p.K1308R or p.M1701V show no significant changes. Data are reported as fold change relative to WT (set to 1), calculated using the 2^−ΔΔCt method and normalized to *SCN4A* to account for transgene expression. WT values are shown without variability, as they represent the reference condition. Data distribution was assessed using the Shapiro–Wilk test. All datasets satisfied normality and were analysed using two-tailed unpaired Student's *t*-test. Values represent mean ± SEM. Significance:* $p < 0.05$; ** $p < 0.01$. $N \geq 3$ independent transfections.

total*XBP1*: 2.42 ± 1.04-fold), while p.M1701V showed *XBP1* levels comparable to WT (s*XBP1*: 1.16 ± 0.81-fold; us*XBP1*: 1.39 ± 1.03-fold; total*XBP1*: 1.25 ± 0.89-fold) (Figs. 3**B**, 3**D**). Neither variant significantly altered *DDIT3*/CHOP (K1308R: 1.62 ± 0.54-fold; M1701V: 1.00 ± 0.61-fold) or *HSPA5*/BiP (K1308R: 1.86 ± 0.74-fold; M1701V: 1.12 ± 0.77-fold) (Figs. 3**F**, 3**G**).

Finally, *ATF4* mRNA levels, despite unstable in the experimental setting, remained unchanged across all variants (p.K1308R: 5.29 ± 4.43-fold; p.R1451H: 3.19 ± 0.82-fold; p.M1701V: 3.41 ± 3.19-fold; relative to WT) (Fig. 3**E**).

3.7. Temperature effect on biophysical parameters

Cold is a well-known trigger for myotonia, while a warm environment can alleviate symptoms [32]. Furthermore, some *SCN4A* variants have been described as having temperature-dependent characteristics [33–35]. Given that both the probands from family 2 and 3 experience worsening with cold temperatures, the p.R1451H and p.M1701V channels were evaluated at 37 °C to access whether increased temperature could improve the behaviour of the mutated channels. At 37 °C (Fig. 4, and Table 2**B**), both variants showed a recovery of the current amplitude, reaching values comparable to those of the WT channel recorded at RT (Fig. 4**A-4B**). As expected, the kinetics of both activation (Fig. 4**C**) and inactivation (Fig. 4**D**) were accelerated. For both variants, the alterations in the voltage dependence of activation observed at RT were no longer present, whereas the changes in the voltage dependence of inactivation persisted (data summarized in Table 2**B**). These results also brought to a change in parameters of the calculated window current, that resulted in an increment of open probability and a more depolarized peak voltage for both variants (Table 2**B**).

3.8. Mexiletine effects on the $Na_V1.4$ channel behaviour

Mexiletine is one of the most effective drugs for myotonia and it is widely used in the treatment of NDMs [2]. To reproduce a steady state effect that chronic treatment has in patients, HEK293T cells overexpressing $Na_V1.4$ WT or the three variants were incubated for 24 hs with 0.1 mM mexiletine, and patch-clamp recordings were then performed at RT. A summary of the experimental data is presented in Fig. 5, Table 2**C**, and Supplementary Figure S6.

Mexiletine treatment had a different impact on the three $Na_V1.4$ variants. A significant reduction in current density was observed only for p.R1451H (Figs. 5**D**, 5**J**), whereas no change for p.K1308R and p.M1701V. Despite this, the drug altered the voltage dependence of activation and inactivation across all constructs, although with variant-specific patterns (Figs. 5**B**, 5**E**, 5**H**). In p.K1308R and p.M1701V, both activation and inactivation curves shifted toward more depolarized potentials; in p.R1451H, it induced a further depolarizing shift of the activation curve without affecting inactivation. The corresponding calculated window currents are shown in Figs. 5**C**, 5**F**, 5**I**. Mexiletine incubation produced a modest reduction in open probability in all variants and displaced the peak of the window current toward values closer

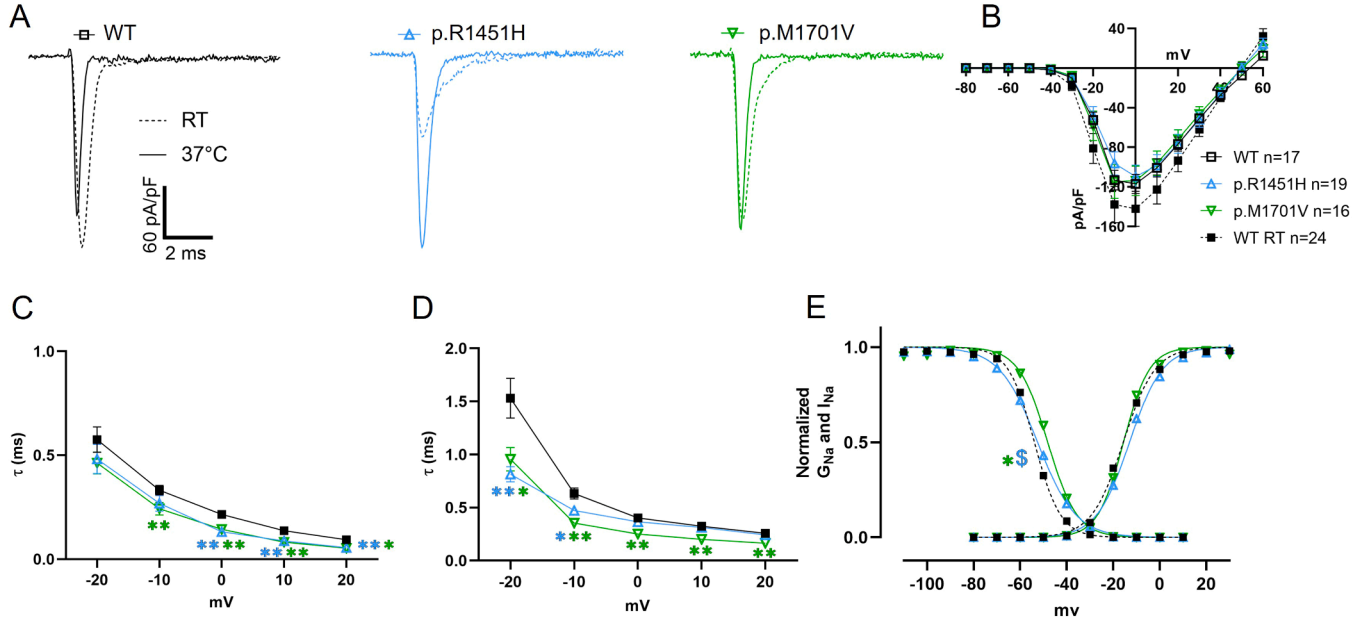

Fig. 4. Temperature-mediated effects on p.R1451H and p.M1701V. (A) Representative current traces of $Na_V1.4$ channels recorded at 37°C under whole-cell patch-clamp configuration. Traces are shown for the WT (black, solid line), p.R1451H (blue, solid line), and p.M1701V (green, solid line) variants. The dotted line indicates an average representative trace recorded at RT, for comparison. (B) Current–voltage (I–V) relationships illustrating the sodium current density across the whole range of voltage tested, measured at 37 °C (open symbols) compared to the WT channel at RT (black, filled squares). (C) Kinetics of channel activation and (D) channel fast inactivation calculated as described in the Patients and Methods section. (E) Activation and inactivation curves fitted using the Boltzmann equation. Data are shown as mean ± SEM and summarized in Table 2B. Statistical significance: * $p < 0.05$, $ $p < 0.05$ indicates the difference in the slope factor k, ** $p < 0.01$, *t*-test analysis. Statistical symbols are color-coded to match the colours assigned to each mutation.

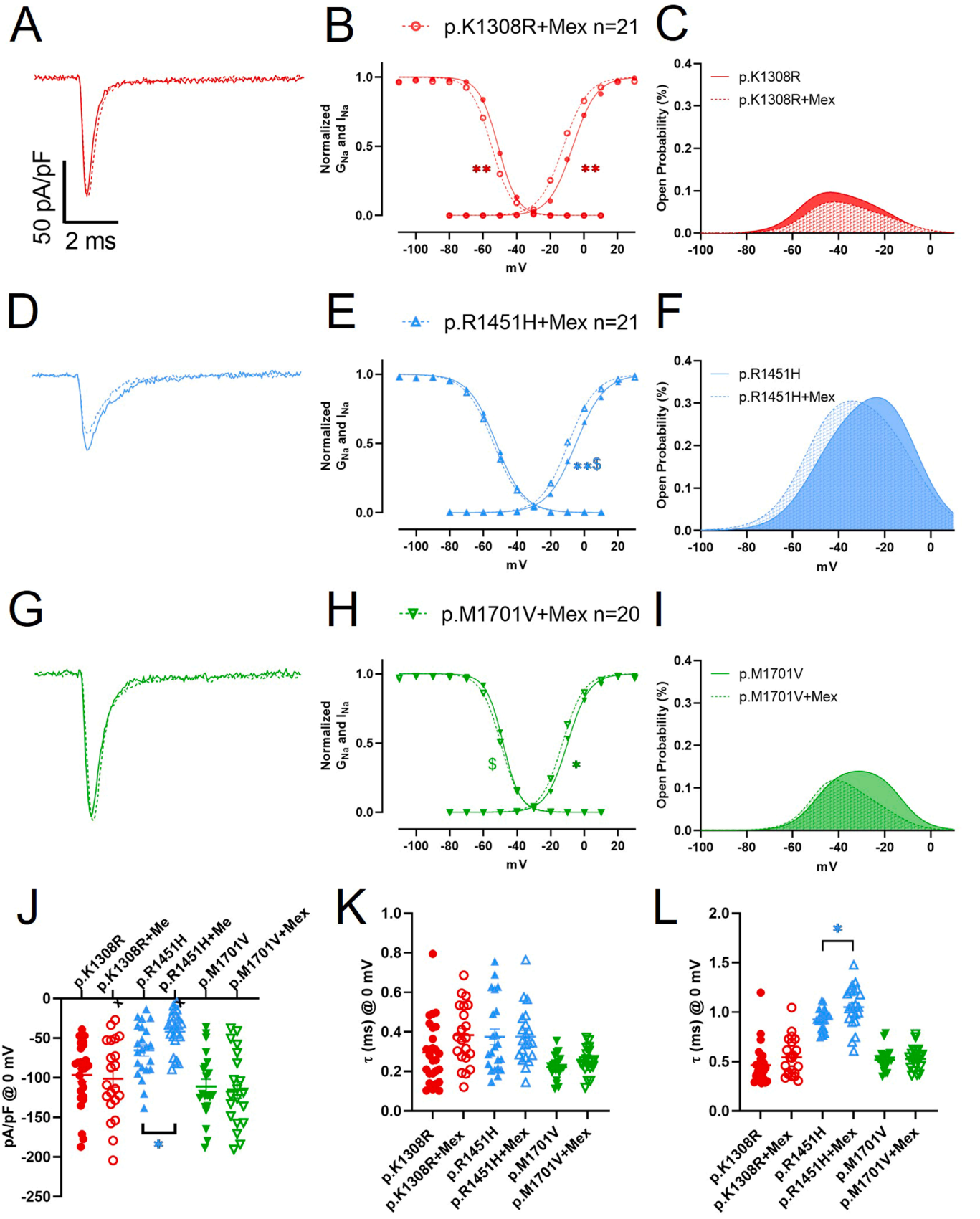

(caption on next page)

Fig. 5. Effects of 24 h incubation with mexiletine (0.1 mM) on the $Na_V1.4$ variants. (A, D, G) Representative peak current traces in response to a depolarizing pulse to 0 mV for p.K1308R (red), p.R1451H (blue), and p.M1701V (green), respectively. Traces represent the averaged recordings from all cells under each condition. Solid lines correspond to control conditions, while dotted lines correspond to recordings after mexiletine incubation (see Table 2 for values). Control and mexiletine-treated recordings were obtained from separate groups of cells. (B, E, H) Activation and inactivation curves were fitted with the Boltzmann equation. Open symbols indicate measurements obtained after mexiletine incubation, whereas filled symbols refer to untreated cells. Data are presented as mean ± SEM and summarized in Table 2C. Statistical significance: * $p < 0.05$; ** $p < 0.0$; $ $p < 0.05$ indicates the difference in the slope factor k; vs the corresponding variant recorded without mexiletine (*t*-test). (C, F, I) Calculated window currents expressed as open probability (see Patients and Methods and Table 2C for summarized data). (J, K, L) Scatter plots showing the distribution of the current density values recorded at 0 mV, the kinetics of channel activation and the kinetics of inactivation, respectively, obtained in absence (filled symbols) and in presence (empty symbols) of mexiletine. The black line represents the average values. Data are presented as mean ± SEM and summarized in Table 2C.

to those of the WT channel. Activation and inactivation kinetics, quantified at 0 mV, are reported in Figs. 5**K and** 5**L**. Mexiletine did not modify the former, but specifically slowed the fast inactivation in the p.R1451H variant. For completeness, the same analyses of the drug effects were performed on $Na_V1.4$ WT and reported in the Supplementary Materials (Supplementary Figure S6**)** and data are summarized in Table 2**C**. Given that the p.R1451H variant is associated with pronounced ER stress and impaired membrane trafficking, a possible restorative effect of mexiletine on these cellular alterations was investigated. However, immunofluorescence analysis in HEK293T cells expressing p.R1451H and treated for 24 hs with 0.1 mM mexiletine did not reveal appreciable differences compared to untreated cells, in terms of either overall expression levels or membrane localization of the channel (Supplementary Figure S7, **A-D**). Consistently, qPCR analysis of ER stress–related markers showed no relevant changes upon drug treatment, indicating that mexiletine does not significantly modulate the unfolded protein response under these conditions (Supplementary Figure S7, **E-J**). Overall, these findings suggest that chronic exposure to mexiletine does not rescue trafficking defects nor exacerbate ER stress in cells expressing the p.R1451H variant.

Finally, since in patients the duration of beneficial drug effects matches mexiletine half-life, suggesting that steady-state effects may contribute only partially to the overall benefit, its acute effect was further investigated to assess its potential contribution. To this aim, $Na_V1.4$ sodium currents, WT or the three variants, were recorded using a use-dependent block protocol (test pulses at 10 Hz) under continuous superfusion with 0.1 mM mexiletine, in order to mimic acute drug exposure. The results are reported in Supplementary Figure S8 and Table 2**D**. As expected, mexiletine consistently reduced sodium current in all tested conditions, in line with its known inhibitory action on sodium channels. Interestingly, the effect was more prominent in the p.K1308R and p.R1451H, suggesting an increase in sensitivity in these two mutated channels.

3.9. Reclassification of SCN4A variants after functional studies

The results of functional studies conducted on HEK293T cells expressing channels carrying the variants under analysis led to a reclassification for the p.K1308R and p.M1701V variants. p.K1308R was reclassified as likely pathogenic (PS3, PM1, PM2_sup), while p.M1701V was reclassified as likely pathogenic (PS3, PM2_sup, PP1, PP3).

4. Discussion

4.1. Functional interpretation of variants

In this study, we combined clinical assessments, genetic analysis, and comprehensive functional characterization to investigate three *SCN4A* variants - c.3923 A>G, c.4352 G>A, and c.5101 A>G - resulting in $Na_V1.4$ missense mutations p.K1308R, p.R1451H, and p.M1701V, respectively, identified in unrelated families presenting with NDM of variable severity. These variants were all predicted to be pathogenic by in silico tools and were absent or extremely rare in population databases. Notably, all probands also harboured the heterozygous *CLCN1* c.568_569delinsTC, a well-established mutation (p.G190S), first reported in a consanguineous Arab family, both in heterozygous and homozygous states [35] and frequently found in Italian patients with myotonia congenita [8–10]. Functional studies demonstrated that p.G190S markedly reduces chloride conductance by decreasing channel open probability [9;20], confirming its pathogenic role. The coexistence of deleterious variants in both *SCN4A* and *CLCN1* likely contributes to the phenotypic variability observed among affected individuals. Here, we provide mechanistic evidence demonstrating that each *SCN4A* variant, when overexpressed in HEK293T cells, produced a distinct constellation of biophysical changes that may collectively contribute to both shared and divergent clinical features among carriers.

The p.K1308R variant affects a residue within the DIII–DIV linker, positioned between the inactivation gate hinge and the IFMT motif, a key structural element of channel fast inactivation [28,36]. This mutation represents a conservative substitution, replacing one positively charged residue (K) with another one (R). Despite this similarity, the two residues differ in side-chain geometry and interaction potential: arginine's larger and more complex guanidinium group can form more extensive hydrogen-bonding and salt-bridge networks than lysine. This may change the local conformational dynamics of the inactivation gate.

The p.R1451H substitution is non-conservative, replacing a highly conserved, strongly basic arginine with a less basic histidine, thus reducing the positive charge at a critical voltage-sensing residue (DIV-S4). Given the importance of this domain in channel voltage sensing, this modification is expected to reduce the gating charge and weaken the electrostatic interactions that stabilize S4 within the gating pore (such as the one with E1373 in DIV S1 [28]). The R to H substitution may therefore compromise voltage sensing or introduce aberrant voltage-sensor behaviour. The same mutation was already identified in a patient with myalgia and myotonic discharges and partially described as affecting the gating and the kinetics properties [37]. Moreover, this residue seems to be a hot spot since two other missense mutations are located in the same position: p.R1451L and p.R1451C. Both variants have been extensively studied and are described as pathogenic based on electrophysiological studies and clinical phenotypes [38,39].

The p.M1701V variant is a conservative substitution involving two hydrophobic residues of comparable size (Met → Val). Based on residue numbering, M1701 lies within the resolved portion of the C-terminus tail, thus, its side chain is likely part of a region that folds into a defined structure. This suggests that its replacement could affect local folding. Despite the conservative, hydrophobic substitution, the loss of the sulphur in methionine can change side chain volume/flexibility, potentially altering the conformational dynamics of the C-tail of the channel and resulting in mild changes in its functionality.

Despite affecting different channel regions, the three $Na_V1.4$ variants, when overexpressed in HEK293T cells, produced a set of partially overlapping abnormalities. All altered at least one component of the voltage dependence of gating or kinetic behaviour, and two variants (p.K1308R and p.R1451H) caused a marked reduction in current density. Interestingly, reduced peak current was not uniformly attributable to impaired surface expression: while p.R1451H displayed clear membrane retention, p.K1308R preserved normal trafficking, indicating that distinct mechanisms underlie the shared reduction in macroscopic sodium currents.

Gating alterations emerged as the most consistent theme. p.K1308R

and p.R1451H shifted activation toward more depolarized potentials and slowed activation kinetics, whereas p.M1701V primarily affected steady-state inactivation and inactivation kinetics. These differences resulted in variant-specific modifications of window current properties, with p.R1451H and p.M1701V increasing the predicted open probability and shifting the window to more depolarized voltages. In particular, when considering the area under the curve, the p.R1451H variant exhibited an approximately fourfold increase in window current area compared with the WT channel, consistent with findings by Poulin and colleagues [39], who reported similar effects for mutations affecting the same residue. p.K1308R induced only minor changes in the activation curve resulting in a shift of the window current peak in the opposite direction. Such changes are expected to modify membrane excitability in distinct ways. Furthermore, the observed increase in window current may contribute to enhanced membrane excitability, particularly within the range of resting membrane potentials, which could partially explain the myotonic symptoms observed in patients carrying the p.R1451H variant.

Overall, these patterns demonstrate that the three mutations do not fit into a single "loss-of-function" or "gain-of-function" category [40] but instead show hybrid features affecting different aspects of channel gating. In particular, the altered gating kinetics in p.K1308R primarily produces an activation deficit, in p.M1701V primarily perturbs inactivation and window current properties, and p.R1451H exerts broad defects across multiple gating processes. They may all significantly impact muscle excitability by modifying the temporal profile of sodium current during the action potential.

To obtain a more dynamic representation of sodium current contribution, we designed a voltage-clamp protocol that mimics the waveform of a skeletal muscle action potential [41]. The currents recorded with this dynamic protocol effectively recapitulated overall the biophysical alterations previously observed. Indeed, the slower activation kinetics detected in p.K1308R and especially in p.R1451H markedly delayed the depolarization phase compared with WT. p.R1451H variant also resulted in a prolonged contribution in the repolarization phase, as measured at 30% and 50% of the current decay, an effect compatible with its slower kinetics of the fast inactivation and expanded window current. The p.M1701V variant despite sharing this latter feature, contribute less to the repolarization phase of the AP, most likely due to the substantial reduction in the sustained late current generated by this variant.

Our simple analytical protocol provides useful insight into how specific biophysical properties of the sodium current—beyond their steady-state voltage dependence—integrate dynamically and contribute to shaping the action potential. In the WT channel, inspection of the current during the return to resting potential revealed, after the expected steep decline driven by the fast inactivation of the channel, the presence of a plateau-like component. This feature can reasonably be interpreted as the combined contribution of the late and window currents, with the latter emerging in the final portion of the trace, consistent with the voltage at which it peaks. The comparison of this reference profile with those of the mutant channels illustrates how distinct kinetic alterations reshape these contributions. In the p.R1451H variant, the slowed inactivation generates a pronounced shoulder that merges with the window current, whose peak is shifted to more depolarized potentials relative to WT; consequently, the characteristic plateau becomes masked, and the late current contribution is obscured. In contrast, the absence of a plateau in p.M1701V is more consistent with its markedly reduced late current, as its inactivation kinetics remain slow, but its window current exhibits a peak and open probability comparable to WT. The p.K1308R variant, lacking both a prominent late component and a markedly altered window current, displays a profile essentially indistinguishable from WT. Taken together, these observations suggest that the "plateau" seen during repolarization may primarily reflect the presence of late current, whereas the window current - particularly when shifted to depolarized potentials, as previously proposed by Farinato et al. [42] - can modify the sodium-current trajectory during the action potential and thereby enhance membrane excitability. This conceptual framework echoes earlier hypotheses indicating that even subtle shifts in persistent or window components can meaningfully influence excitability dynamics.

In addition, beyond electrophysiology, the overexpression of the proteins in HEK293T cells differentially influenced cells morphology, channel expression and trafficking, and ER stress activation. Cell circularity and aspect ratio are widely used quantitative proxies for cellular status, as changes in cell shape often reflect underlying biological processes. In CHO cells, a more rounded cell aspect may correlate with the activation of the protein synthesis pathway [43]. Of course, these changes, are not diagnostic on their own, but they frequently correlate with specific cellular states. For example, cell rounding or reduced spreading, thus an increased circularity and reduced aspect ratio, may correlate with ER stress, oxidative stress, or membrane trafficking defects [29].

Strikingly, the p.R1451H variant exhibited the most severe cellular impairment among the tested mutants, characterized by pronounced ER retention, and trafficking failure. Cells expressing p.R1451H showed reduced *SCN4A* mRNA, ~50% loss of membrane protein abundance, and markedly diminished fluorescence at the cell surface, consistent with strong intracellular accumulation. Quantification of F_{PN}/F_{PM} ratios confirmed that p.R1451H was the only variant with a robust trafficking deficit, which likely underlies its substantial reduction in surface expression and consequent functional loss. This misprocessing was accompanied by broad activation of the unfolded protein response, with elevated *XBP1* transcripts, impaired *XBP1* splicing efficiency, and increased CHOP and BiP expression, indicating activation of multiple UPR arms [44–46] and suggesting an overwhelmed proteostasis network. The associated morphological rounding and reduced transfection efficiency further support a high proteostatic burden. Notably, p.R1451 is a known mutational hot spot, with several pathogenic substitutions (p.R1451C, p.R1451L) [39] previously linked to loss-of-function channelopathies, underscoring the functional importance of this residue and reinforcing the pathogenic classification of p.R1451H.

In contrast, the p.K1308R and p.M1701V variants exhibited largely preserved expression, trafficking, and proteostatic homeostasis, with only minimal or non-significant changes in ER-stress markers despite subtle alterations in cell morphology. Trafficking analyses showed that p.K1308R maintained normal membrane abundance, indicating that its reduced current density likely arises from altered gating rather than misprocessing. Similarly, p.M1701V displayed normal trafficking and even increased membrane protein levels, consistent with its near-normal peak current density despite measurable biophysical perturbations.

These latter findings, however, should be interpreted with caution, as they were obtained in a heterologous overexpression system rather than in skeletal muscle cells. Therefore, they may not fully reflect the *in vivo* patient context or their direct clinical relevance and cannot be fully extrapolated to the complexity of skeletal myocytes—where regulatory mechanisms, protein interactions, and cellular context differ substantially. Nonetheless, they provide meaningful insight into the intrinsic behaviour of individual channel variants under controlled overexpression conditions. Indeed, such systems remain valuable for distinguishing channel-specific properties from tissue-dependent modulation and for investigating how different molecular defects affect channel processing and function at the cellular level. In this regard, the observed variant-specific differences further underscore how distinct pathogenic mechanisms, including altered folding and trafficking or altered channel gating, may converge toward partially overlapping electrophysiological phenotypes.

4.2. Pharmacological implications

In patients carrying p.R1451H and p.M1701V, symptoms worsen upon exposure to low temperatures, with cold representing a well-

recognized trigger of myotonia, whereas warmth generally alleviates symptoms. To investigate the effects of temperature on channel behaviour, we evaluated the biophysical properties of both variants at 37 °C. Under these conditions, several functional abnormalities were partially reversed, including recovery of current amplitude to levels comparable to WT at room temperature and normalization of the voltage dependence of activation, while defects in inactivation persisted. The increased probability of window currents observed at 37 °C in both variants may reflect a temperature-dependent acceleration of channel gating transitions.

These results indicate that the functional defects associated with p.R1451H and p.M1701V are, at least in part, temperature-sensitive and may arise from destabilization of specific gating states at lower temperatures. This temperature dependence is consistent with the episodic worsening of symptoms reported during cold exposure in affected individuals. The clinical improvement commonly reported in warm environments raises the possibility that sustained exposure to higher ambient temperatures, such as those encountered in warmer climates, may mitigate symptom severity in these patients. In terms of drugs that mitigate the myotonic phenotype, mexiletine is used as first-line treatment option. Across the three variants, chronic mexiletine exposure produced heterogeneous but generally beneficial modulatory effects on channel gating, revealing important pharmacogenetic differences. However, several aspects should be considered when interpreting the effects of mexiletine. Firstly, the concentration used in the present study (0.1 mM) exceeds typical therapeutic plasma levels (~10 μM), although similar concentrations have been widely employed in in-vitro studies investigating both channel block and pharmacological rescue [24,47,48].

Most notably the effects were particularly evident on the parameters defining the window current. The p.R1451H variant, which uniquely displayed a further reduction in current density together with persistently prolonged inactivation kinetics, showed an intensified depolarizing shift in activation upon mexiletine exposure; although this minimally affected the overall window current open probability, it displaced the window peak toward more hyperpolarized potentials, restoring it to values comparable to wild type and thereby mitigating the pathological impact of the window current. A similar trend, though milder, was observed for p.M1701V, which maintained normal current density but exhibited slowed inactivation and a right-shifted activation curve that mexiletine did not fully normalize; nonetheless, the drug produced a slight reduction in window open probability and modest hyperpolarizing shift of the peak. In contrast, p.K1308R preserved current density yet displayed slowed fast inactivation and positive shifts in both activation and inactivation, changes that collectively reduced window current open probability and shifted its peak closer to wild-type values, again reflecting an overall favourable modulation. These observations suggest that chronic exposure to mexiletine primarily acts by reshaping the window current landscape—most prominently in p.R1451H and p.M1701V— toward WT values. Consistently, mexiletine did not improve the cellular impairment caused by the p.R1451H variant, and no restorative effect on trafficking or ER stress markers was detected under chronic exposure conditions. This further support that, at least in this context, its primary action is functional rather than related to correction of protein processing defects. As already previously reported [24; 48] the distinct responses among variants underscore once again the importance of considering mutation-specific properties when evaluating drug efficacy. This is particularly relevant since the magnitude of mexiletine rescue (chronic effect) or block (acute effect) is likely mutation-dependent. In these terms, another aspect to consider is related to the temporal profile of clinical benefit, that closely matches the drug half-life, suggesting that steady-state effects may only partially account for efficacy, while acute use-dependent block is likely to play a major role. This was confirmed by the acute exposure results that revealed, once again, a mutation dependent sensitivity. Thus, the exacerbation of symptoms observed upon treatment interruption may reflect the loss of acute channel inhibition, highlighting the importance of short-term pharmacological effects. In light of all these observations and considerations, additional studies at clinically relevant concentrations will be necessary to dissect the minimum dose capable of preserving chronic beneficial effects while minimizing the acute overall sodium channel block. An interesting parallel line of investigation would be to determine whether mutation-dependent functional rescue similar to that observed with chronic mexiletine exposure may also be achieved with other sodium channel blockers, particularly compounds with greater selectivity for $Na_V1.4$. In this context, μ-conotoxins represent especially attractive candidates, as several members of this peptide family derived from Conus venoms show a remarkable ability to discriminate among closely related sodium channel isoforms and display high affinity for the skeletal muscle channel [49–52]. For example, μ-conotoxin GIIIA and related analogues preferentially inhibit $Na_V1.4$ over neuronal subtypes, while peptides such as SxIIIA/SxIIIB exhibit even stronger selectivity for the skeletal muscle isoform [51]. Although these compounds are classically considered pore blockers, their highly specific channel–toxin interactions may also provide a framework for exploring whether prolonged or controlled exposure can induce beneficial state-dependent modulation of mutant channels, as observed here with mexiletine. Such studies could open new perspectives for mutation-tailored pharmacological strategies in skeletal muscle channelopathies.

4.3. Clinical correlations and implications

The mechanistic signatures revealed by our functional and cellular analyses unravel the complexity of the molecular mechanisms involved by each pathogenic or likely pathogenic variant in causing disease. The p.K1308R variant produced a relatively mild channelopathy centred on activation defects, consistent with classical myotonia. The p.R1451H variant caused profound gating and trafficking abnormalities and elicited substantial proteostatic stress correlating with a more severe phenotype when present together with CLCN1 p.G190S. The p.M1701V variant resulted in moderate gating impairment with preserved expression, aligning with a milder, predominantly cold-induced phenotype.

Unusual clinical phenotypes have been associated with pathogenic variants affecting R1451. The p.R1451H variant caused a myalgic phenotype with myotonic discharges on EMG in a patient who presented with muscle cramps [36] and severe muscle pain and myotonia in a patient in whom this variant coexists with myotonic dystrophy type 2 [53]. The patient carrying the p.R1451C experienced an attack of hypokalemic periodic paralysis (hypoPP) triggered by a glucocorticoid injection the day after a carbohydrate-rich meal [38], while patients carrying p.R1451L showed different phenotypes, such as cold-induced myotonia, a mixed phenotype of hypo- and hyper-PP [38] or a mixed phenotype of hypoPP and myotonia in a homozygous patient (37). HypoPP is caused by substitution of S4 arginines in one of the first three domains of Nav1.4 that induces gating pore currents through the voltage sensor domain [54]. Patients carrying the p.R1451H showed a myotonic and/or myalgic phenotype without episodes of paralysis. This is consistent with previous findings that replacing arginine 1451 with a histidine does not induce gating pore currents [55]. Functional studies have also excluded the hypothesis that p.R1451L could conduct a gating pore current, suggesting that the pathomechanism causing the hypoPP phenotype presented by these patients should be different [38]. The unusual clinical presentations in patients carrying the p.R1451C/H/L variants is likely due to the association of the intrinsic properties of the mutated channels combined with additional factors influencing the phenotype.

Importantly, the co-occurrence of the *CLCN1* p.G190S variant in all probands of this study likely amplified clinical severity. Dual impairment of sodium and chloride homeostasis reduces membrane stability, facilitating after-discharges [56] and exacerbating cold sensitivity.

These findings highlight the importance of considering digenic or multigenic contributions when interpreting genotype–phenotype relationships in NDM.

5. Conclusions

These findings demonstrate that clinically similar myotonic phenotypes caused by *SCN4A* pathogenic variants can arise from markedly distinct molecular mechanisms. The coexistence of pathogenic *CLCN1* variants, which may further modify clinical expressivity [17], highlights the complexity of genotype–phenotype correlations in skeletal muscle channelopathies. In this context, the integration of electrophysiology, cell biology, and pharmacological profiling proved essential for interpreting the pathogenicity of $Na_V1.4$ variants and may ultimately facilitate more accurate variant reclassification. Collectively, the experimental framework adopted here provides a useful reference for interpreting variant behaviour across different experimental systems and for future studies aimed at defining variant-specific functional consequences.

The divergent responses to mexiletine further suggest that individual variants may require tailored therapeutic strategies rather than uniform application of sodium channel blockers. Likewise, the temperature sensitivity observed for p.R1451H and p.M1701V supports a role for thermal modulation in symptom management. In addition, the marked ER-stress phenotype associated with p.R1451H, despite being observed in a heterologous model, raises the possibility that proteostasis-targeting approaches could represent a therapeutic avenue in selected cases. Finally, to our knowledge, this is the first study demonstrating that impaired $Na_V1.4$ trafficking may contribute to the pathogenesis of myotonia.

CRediT authorship contribution statement

Comi Giacomo P: Funding acquisition. **Luigi Anastasia:** Writing – review & editing, Funding acquisition. **Anthony Frosio:** Writing – original draft, Methodology, Formal analysis, Data curation. **Serena Calamaio:** Writing – original draft, Methodology, Formal analysis, Data curation. **Serena Pagliarani:** Writing – original draft, Methodology, Formal analysis, Data curation. **Giovanni Meola:** Writing – review & editing, Funding acquisition. **Federica Cirillo:** Writing – original draft, Methodology, Formal analysis, Data curation. **Ilaria Rivolta:** Writing – review & editing, Supervision, Funding acquisition, Conceptualization. **Dario Melgari:** Writing – review & editing, Methodology, Formal analysis. **Rachele Prevostini:** Formal analysis. **Lo Presti Franceca:** Formal analysis. **Sabrina Lucchiari:** Methodology. **Francesca Magri:** Writing – review & editing, Writing – original draft. **Stefania Corti:** Funding acquisition. **Carlo Pappone:** Writing – review & editing, Funding acquisition.

Declaration of Competing Interest

All authors of the presente manuscript disclose any financial and personal relationships with other people or organizations that could inappropriately influence or bias their work.

Acknowledgments

Special thanks to “Associazione Centro Dino Ferrari”, Milan, Italy, and to FMM-Fondazione Malattie Miotoniche ETS-FMMETS, Milan, Italy, for their support. We acknowledge the Italian Ministry of Health for partially funding this work (Ricerca Corrente to IRCCS Policlinico San Donato) and IRCCS Policlinico San Donato for own funds. The authors acknowledge the use of the free version of ChatGPT (OpenAI) only for grammar, style, and language refinement. The tool did not have access to any research data and was not used for data processing, statistical analysis, or the development of scientific arguments or conclusions.

Appendix A. Supporting information

Supplementary data associated with this article can be found in the online version at doi:10.1016/j.biopha.2026.119625.

Data Availability

Data will be made available on request.

References

[1] E. Matthews, D. Fialho, S.V. Tan, S.L. Venance, S.C. Cannon, D. Sternberg, B. Fontaine, A.A. Amato, R.J. Barohn, R.C. Griggs, M.G. Hanna, CINCH Investigators. The non-dystrophic myotonias: molecular pathogenesis, diagnosis and treatment, Brain 133 (Pt 1) (2010) 9–22, https://doi.org/10.1093/brain/awp294.

[2] B.C. Stunnenberg, S. LoRusso, W.D. Arnold, R.J. Barohn, S.C. Cannon, B. Fontaine, R.C. Griggs, M.G. Hanna, E. Matthews, G. Meola, V.A. Sansone, J.R. Trivedi, B.G. M. van Engelen, S. Vicart, J.M. Statland, Guidelines on clinical presentation and management of nondystrophic myotonias, Muscle Nerve 62 (4) (2020) 430–444, https://doi.org/10.1002/mus.26887.

[3] V. Vivekanandam, R. Jaibaji, R. Sud, R. Ellmers, I. Skorupinska, L. Germaine, N. James, S. Holmes, R. Mannikko, D. Jayaseelan, M.G. Hanna, Prevalence of genetically confirmed skeletal muscle channelopathies in the era of next generation sequencing, Neuromuscul. Disord. 33 (3) (2023) 270–273, https://doi.org/10.1016/j.nmd.2023.01.007.

[4] I. Saltarella, P. Laghetti, S. Dell'Atti, C. Altamura, J.F. Desaphy, Pharmacological therapy of non-dystrophic myotonias, Acta Myol. 44 (1) (2025) 23–27, https://doi.org/10.36185/2532-1900-1026.

[5] J. Spillane, J. Trip, G. Drost, C.G. Faber, M.G. Hanna, S.J. Nevitt, V. Vivekanandam, Drug treatment for myotonia, Cochrane Database Syst. Rev. 4 (4) (2025) CD004762, https://doi.org/10.1002/14651858.CD004762.pub3.

[6] K.J. Suetterlin, E. Bugiardini, J.P. Kaski, J.M. Morrow, E. Matthews, M.G. Hanna, D. Fialho, Long-term Safety and Efficacy of Mexiletine for Patients With Skeletal Muscle Channelopathies, JAMA Neurol. 72 (12) (2015) 1531–1533, https://doi.org/10.1001/jamaneurol.2015.2338.

[7] A. Modoni, A. D'Amico, G. Primiano, F. Capozzoli, J.F. Desaphy, M. Lo Monaco, Long-Term Safety and Usefulness of Mexiletine in a Large Cohort of Patients Affected by Non-dystrophic Myotonias, Front. Neurol. 11 (2020) 300, https://doi.org/10.3389/fneur.2020.00300.

[8] A. Modoni, A. D'Amico, B. Dallapiccola, M.L. Mereu, L. Merlini, S. Pagliarani, E. Pisaneschi, G. Silvestri, I. Torrente, E.M. Valente, M. Lo Monaco, Low-rate repetitive nerve stimulation protocol in an Italian cohort of patients affected by recessive myotonia congenita, J. Clin. Neurophysiol. 28 (1) (2011) 39–44, https://doi.org/10.1097/WNP.0b013e31820510d7.

[9] G. Ulzi, M. Lecchi, V. Sansone, E. Redaelli, E. Corti, D. Saccomanno, S. Pagliarani, S. Corti, F. Magri, M. Raimondi, G. D'Angelo, A. Modoni, N. Bresolin, G. Meola, E. Wanke, G.P. Comi, S. Lucchiari, Myotonia congenita: novel mutations in CLCN1 gene and functional characterizations in Italian patients, J. Neurol. Sci. 318 (1-2) (2012) 65–71, https://doi.org/10.1016/j.jns.2012.03.024.

[10] R. Brugnoni, D. Kapetis, P. Imbrici, M. Pessia, E. Canioni, L. Colleoni, N.K. de Rosbo, L. Morandi, P. Cudia, N. Gashemi, P. Bernasconi, J.F. Desaphy, D. Conte, R. Mantegazza, A large cohort of myotonia congenita probands: novel mutations and a high-frequency mutation region in exons 4 and 5 of the CLCN1 gene, J. Hum. Genet. 58 (9) (2013) 581–587, https://doi.org/10.1038/jhg.2013.58.

[11] S. Portaro, C. Altamura, N. Licata, G.M. Camerino, P. Imbrici, O. Musumeci, C. Rodolico, D. Conte Camerino, A. Toscano, J.F. Desaphy, Clinical, Molecular, and Functional Characterization of CLCN1 Mutations in Three Families with Recessive Myotonia Congenita, Neuromolecular Med. 17 (3) (2015) 285–296, https://doi.org/10.1007/s12017-015-8356-8.

[12] V. Ferradini, M. Cassone, S. Nuovo, I. Bagni, M.R. D'Apice, A. Botta, G. Novelli, F. Sangiuolo, Targeted Next Generation Sequencing in patients with Myotonia Congenita, Clin. Chim. Acta 470 (2017) 1–7, https://doi.org/10.1016/j.cca.2017.04.012.

[13] C. Orsini, R. Petillo, P. D'Ambrosio, M. Ergoli, E. Picillo, M. Scutifero, L. Passamano, A. De Luca, L. Politano, *CLCN1* Molecular Characterization in 19 South-Italian Patients With Dominant and Recessive Type of Myotonia Congenita, Front. Neurol. 11 (2020) 63, https://doi.org/10.3389/fneur.2020.00063.

[14] A. Furby, S. Vicart, J.P. Camdessanché, E. Fournier, S. Chabrier, E. Lagrue, C. Paricio, P. Blondy, R. Touraine, D. Sternberg, B. Fontaine, Heterozygous CLCN1 mutations can modulate phenotype in sodium channel myotonia, Neuromuscul. Disord. 24 (11) (2014) 953–959, https://doi.org/10.1016/j.nmd.2014.06.439.

[15] C. Zhao, D. Tang, H. Huang, H. Tang, Y. Yang, M. Yang, Y. Luo, H. Tao, J. Tang, X. Zhou, X. Shi, Myotonia congenita and periodic hypokalemia paralysis in a consanguineous marriage pedigree: Coexistence of a novel CLCN1 mutation and an SCN4A mutation, PLoS. One 15 (5) (2020) e0233017, https://doi.org/10.1371/journal.pone.0233017.

[16] S. Pagliarani, G. Meola, M. Filareti, G.P. Comi, S. Lucchiari, Case report: Sodium and chloride muscle channelopathy coexistence: A complicated phenotype and a

challenging diagnosis, Front. Neurol. 13 (2022) 845383, https://doi.org/10.3389/fneur.2022.845383. PMID: 36081873; PMCID: PMC9447429.
[17] V. Vacchiano, R. Brugnoni, C. Campanale, P. Imbrici, G. Dinoi, E. Canioni, P. Laghetti, I. Saltarella, C. Altamura, L. Maggi, R. Liguori, V. Donadio, J. F. Desaphy, Coexistence of SCN4A and CLCN1 mutations in a family with atypical myotonic features: A clinical and functional study, Exp. Neurol. 362 (2023) 114342, https://doi.org/10.1016/j.expneurol.2023.114342.
[18] A. Binda, L.V. Renna, F. Bosè, E. Brigonzi, A. Botta, R. Valaperta, B. Fossati, I. Rivolta, G. Meola, R. Cardani, SCN4A as modifier gene in patients with myotonic dystrophy type 2, Sci. Rep. 8 (1) (2018) 11058, https://doi.org/10.1038/s41598-018-29302-z.
[19] J.H. Yuan, Y. Higuchi, A. Hashiguchi, M. Ando, A. Yoshimura, T. Nakamura, Y. Sakiyama, H. Takashima, Genetic spectrum and founder effect of non-dystrophic myotonia: a Japanese case series study, J. Neurol. 269 (12) (2022) 6406–6415, https://doi.org/10.1007/s00415-022-11305-6.
[20] J.F. Desaphy, G. Gramegna, C. Altamura, M.M. Dinardo, P. Imbrici, A.L. George, Jr, A. Modoni, M. Lomonaco, D. Conte Camerino, Functional characterization of ClC-1 mutations from patients affected by recessive myotonia congenita presenting with different clinical phenotypes, Exp. Neurol. 248 (2013) 530–540, https://doi.org/10.1016/j.expneurol.2013.07.018.
[21] S. Pagliarani, S. Lucchiari, M. Scarlato, E. Redaelli, A. Modoni, F. Magri, B. Fossati, S.C. Previtali, V.A. Sansone, M. Lecchi, M. Lo Monaco, G. Meola, G.P. Comi, Sodium Channel Myotonia Due to Novel Mutations in Domain I of $Na_v1.4$, Front. Neurol. 11 (2020) 255, https://doi.org/10.3389/fneur.2020.00255.
[22] Q. Plumereau, S. Lile, C.N. Johnson, M. Chahine, Biophysical and structural insights into the SCN4A E452K variant linked to myotonia and paramyotonia congenita, Sci. Rep. 15 (1) (2025) 33101, https://doi.org/10.1038/s41598-025-17816-2.
[23] H. Poulin, M. Chahine, R1617Q epilepsy mutation slows Na_V 1.6 sodium channel inactivation and increases the persistent current and neuronal firing, J. Physiol. 599 (5) (2021) 1651–1664, https://doi.org/10.1113/JP280838.
[24] A. Frosio, E. Micaglio, I. Polsinelli, S. Calamaio, D. Melgari, R. Prevostini, A. Ghiroldi, A. Binda, P. Carrera, M. Villa, F. Mastrocinque, S. Presi, R. Salerno, A. Boccellino, L. Anastasia, G. Ciconte, S. Ricagno, C. Pappone, I. Rivolta, Unravelling Novel SCN5A Mutations Linked to Brugada Syndrome: Functional, Structural, and Genetic Insights, Int. J. Mol. Sci. 24 (20) (2023) 15089, https://doi.org/10.3390/ijms242015089.
[25] E.R. Zanier, S. Fumagalli, C. Perego, F. Pischiutta, M.G. De Simoni, Shape descriptors of the "never resting" microglia in three different acute brain injury models in mice, Intensive Care Med. Exp. 3 (1) (2015) 39, https://doi.org/10.1186/s40635-015-0039-0.
[26] A.M. Vela-Alcántara, J. Santiago-García, M. Barragán-Palacios, A. León-Chacón, M. Domínguez-Pantoja, I. Barceinas-Dávila, E. Juárez-Aguilar, E. Tamariz, Differential modulation of cell morphology, migration, and Neuropilin-1 expression in cancer and non-cancer cell lines by substrate stiffness, Front. Cell. Dev. Biol. 12 (2024) 1352233, https://doi.org/10.3389/fcell.2024.1352233.
[27] C.M. Oslowski, F. Urano, Measuring ER stress and the unfolded protein response using mammalian tissue culture system, Methods Enzymol. 490 (2011) 71–92, https://doi.org/10.1016/B978-0-12-385114-7.00004-0.
[28] X. Pan, Z. Li, Q. Zhou, H. Shen, K. Wu, X. Huang, J. Chen, J. Zhang, X. Zhu, J. Lei, W. Xiong, H. Gong, B. Xiao, N. Yan, Structure of the human voltage-gated sodium channel Nav1.4 in complex with β1, Science 362 (6412) (2018) eaau2486, https://doi.org/10.1126/science.aau2486.
[29] L. Gruber, M. Jobst, E. Kiss, M. Karasová, B. Englinger, W. Berger, G. Del Favero, Intracellular remodeling associated with endoplasmic reticulum stress modifies biomechanical compliance of bladder cells, Cell. Commun. Signal. 21 (1) (2023) 307, https://doi.org/10.1186/s12964-023-01295-x.
[30] J. Han, S.H. Back, J. Hur, Y.H. Lin, R. Gildersleeve, J. Shan, C.L. Yuan, D. Krokowski, S. Wang, M. Hatzoglou, M.S. Kilberg, M.A. Sartor, R.J. Kaufman, ER-stress-induced transcriptional regulation increases protein synthesis leading to cell death, Nat. Cell. Biol. 15 (5) (2013) 481–490, https://doi.org/10.1038/ncb2738.
[31] A. Almanza, A. Carlesso, C. Chintha, S. Creedican, D. Doultsinos, B. Leuzzi, A. Luís, N. McCarthy, L. Montibeller, S. More, A. Papaioannou, F. Püschel, M.L. Sassano, J. Skoko, P. Agostinis, J. de Belleroche, L.A. Eriksson, S. Fulda, A.M. Gorman, S. Healy, A. Kozlov, C. Muñoz-Pinedo, M. Rehm, E. Chevet, A. Samali, Endoplasmic reticulum stress signalling - from basic mechanisms to clinical applications, FEBS J. 286 (2) (2019) 241–278, https://doi.org/10.1111/febs.14608.
[32] E. Matthews, S. Holmes, D. Fialho, Skeletal muscle channelopathies: a guide to diagnosis and management, Pract. Neurol. 21 (3) (2021) 196–204, https://doi.org/10.1136/practneurol-2020-002576.
[33] Y. Sugiura, N. Makita, L. Li, P.J. Noble, J. Kimura, Y. Kumagai, T. Soeda, T. Yamamoto, Cold induces shifts of voltage dependence in mutant SCN4A, causing hypokalemic periodic paralysis, Neurology 61 (7) (2003) 914–918, https://doi.org/10.1212/01.wnl.0000086820.54065.a0.
[34] J. Webb, S.C. Cannon, Cold-induced defects of sodium channel gating in atypical periodic paralysis plus myotonia, Neurology 70 (10) (2008) 755–761, https://doi.org/10.1212/01.wnl.0000265397.70057.d8.
[35] A. Shalata, H. Furman, V. Adir, N. Adir, Y. Hujeirat, S.A. Shalev, Z.U. Borochowitz, Myotonia congenita in a large consanguineous Arab family: insight into the clinical spectrum of carriers and double heterozygotes of a novel mutation in the chloride channel CLCN1 gene, Muscle Nerve 41 (4) (2010) 464–469, https://doi.org/10.1002/mus.21525.
[36] J.R. Groome, M.C. Dice, E. Fujimoto, P.C. Ruben, Charge immobilization of skeletal muscle Na+ channels: role of residues in the inactivation linker, Biophys. J. 93 (2007) 1519–1533, https://doi.org/10.1529/biophysj.106.102079.
[37] Perivita Periviita, V. Männikkö, R. Jokela, M. Sud, R. Hanna, M.G. Udd, B. Palmio, J. Novel SCN4A Variants Associated With Myalgic Myotonic Disorder or Paramyotonia, Eur. J. Neurol. 32 (5) (2025) e70157, https://doi.org/10.1111/ene.70157.
[38] S. Luo, M. Sampedro Castañeda, E. Matthews, R. Sud, M.G. Hanna, J. Sun, J. Song, J. Lu, K. Qiao, C. Zhao, R. Männikkö, Hypokalaemic periodic paralysis and myotonia in a patient with homozygous mutation p.R1451L in $Na_V1.4$, Sci. Rep. 8 (1) (2018) 9714, https://doi.org/10.1038/s41598-018-27822-2.
[39] H. Poulin, P. Gosselin-Badaroudine, S. Vicart, K. Habbout, D. Sternberg, S. Giuliano, B. Fontaine, S. Bendahhou, S. Nicole, M. Chahine, Substitutions of the S4DIV R2 residue (R1451) in $Na_V1.4$ lead to complex forms of paramyotonia congenita and periodic paralyses, Sci. Rep. 8 (1) (2018) 2041, https://doi.org/10.1038/s41598-018-20468-0.
[40] S. Senneff, M.M. Lowery, Effects of extracellular potassium on calcium handling and force generation in a model of excitation-contraction coupling in skeletal muscle, J. Theor. Biol. 519 (2021) 110656, https://doi.org/10.1016/j.jtbi.2021.110656.
[41] M. Mantegazza, S. Cestèle, W.A. Catterall, Sodium channelopathies of skeletal muscle and brain, Physiol. Rev. 101 (4) (2021) 1633–1689, https://doi.org/10.1152/physrev.00025.2020.
[42] A. Farinato, C. Altamura, P. Imbrici, L. Maggi, P. Bernasconi, R. Mantegazza, L. Pasquali, G. Siciliano, M. Lo Monaco, C. Vial, D. Sternberg, M.R. Carratù, D. Conte, J.F. Desaphy, Pharmacogenetics of myotonic hNav1.4 sodium channel variants situated near the fast inactivation gate, Pharmacol. Res. 141 (2019) 224–235, https://doi.org/10.1016/j.phrs.2019.01.004.
[43] M. Schwendy, R.E. Unger, M. Bonn, S.H. Parekh, Automated cell segmentation in FIJI® using the DRAQ5 nuclear dye, BMC Bioinforma. 20 (1) (2019) 39, https://doi.org/10.1186/s12859-019-2602-2.
[44] K.P. Lee, M. Dey, D. Neculai, C. Cao, T.E. Dever, F. Sicheri, Structure of the dual enzyme Ire1 reveals the basis for catalysis and regulation in nonconventional RNA splicing, Cell 132 (1) (2008) 89–100, https://doi.org/10.1016/j.cell.2007.10.057.
[45] H.P. Harding, Y. Zhang, D. Ron, Protein translation and folding are coupled by an endoplasmic-reticulum-resident kinase, Nature 397 (6716) (1999) 271–274, https://doi.org/10.1038/16729.
[46] H. Yoshida, T. Matsui, N. Hosokawa, R.J. Kaufman, K. Nagata, K. Mori, A time-dependent phase shift in the mammalian unfolded protein response, Dev. Cell. 4 (2) (2003) 265–271, https://doi.org/10.1016/s1534-5807(03)00022-4.
[47] M.P. Takahashi, S.C. Cannon, Mexiletine block of disease-associated mutations in S6 segments of the human skeletal muscle Na(+) channel, J. Physiol. 537 (Pt 3) (2001) 701–714, https://doi.org/10.1111/j.1469-7793.2001.00701.x.
[48] A. Moreau, D.I. Keller, H. Huang, V. Fressart, C. Schmied, Q. Timour, M. Chahine, Mexiletine differentially restores the trafficking defects caused by two brugada syndrome mutations, Front. Pharmacol. 3 (2012) 62, https://doi.org/10.3389/fphar.2012.00062.
[49] J.R. McArthur, G. Singh, D. McMaster, R. Winkfein, D.P. Tieleman, R.J. French, Interactions of key charged residues contributing to selective block of neuronal sodium channels by μ-conotoxin KIIIA, Mol. Pharmacol. 80 (4) (2011) 573–584, https://doi.org/10.1124/mol.111.073460.
[50] R.J. French, H. Terlau, Sodium channel toxins–receptor targeting and therapeutic potential, Curr. Med. Chem. 11 (23) (2004) 3053–3064, https://doi.org/10.2174/0929867043363866.
[51] B.R. Green, G. Bulaj, R.S. Norton, Structure and function of μ-conotoxins, peptide-based sodium channel blockers with analgesic activity, Future Med. Chem. 6 (15) (2014) 1677–1698, https://doi.org/10.4155/fmc.14.107.
[52] P. Favreau, E. Benoit, H.G. Hocking, L. Carlier, D. D' hoedt, E. Leipold, R. Markgraf, S. Schlumberger, M.A. Córdova, H. Gaertner, M. Paolini-Bertrand, O. Hartley, J. Tytgat, S.H. Heinemann, D. Bertrand, R. Boelens, R. Stöcklin, J. Molgó, A novel μ-conopeptide, CnIIIC, exerts potent and preferential inhibition of NaV1.2/1.4 channels and blocks neuronal nicotinic acetylcholine receptors, Br. J. Pharmacol. 166 (5) (2012) 1654–1668, https://doi.org/10.1111/j.1476-5381.2012.01837.x.
[53] S.C. Cannon, Periodic paralysis, Handb. Clin. Neurol. 203 (2024) 39–58, https://doi.org/10.1016/B978-0-323-90820-7.00002-1.
[54] V.A. Sansone, The Dystrophic and Nondystrophic Myotonias, 6, Muscle and Neuromuscular Junction Disorders, Contin. (Minneap. Minn.) 22 (2016) 1889–1915, https://doi.org/10.1212/CON.0000000000000414.
[55] P. Gosselin-Badaroudine, L. Delemotte, A. Moreau, M.L. Klein, M. Chahine, Gating pore currents and the resting state of Nav1.4 voltage sensor domains, Proc. Natl. Acad. Sci. USA 109 (47) (2012) 19250–19255, https://doi.org/10.1073/pnas.1217990109.
[56] J. Gallaher, M. Bier, J. Siegenbeek van Heukelom, The role of chloride transport in the control of the membrane potential in skeletal muscle–theory and experiment, Biophys. Chem. 143 (1-2) (2009 Jul) 18–25, https://doi.org/10.1016/j.bpc.2009.03.008.